TÉCNICO LISBOA

Identification of Faults and Potential Faults in Low Voltage Lines

Gonçalo Ferreira Gil

Thesis to obtain the Master of Science Degree in

Electrical and Computer Engineering

Supervisor: Prof. Paulo José da Costa Branco

Examination Committee

Chairperson: Prof. Célia Maria Santos Cardoso de Jesus
Supervisor: Prof. Paulo José da Costa Branco
Member of the Committee: Dr. José Eduardo Gomes Oliveira

December 2020

Declaration

I declare that this document is an original work of my own authorship and that it fulfills all the requirements of the Code of Conduct and Good Practices of the Universidade de Lisboa.

Acknowledgments

In the first place, I would like to acknowledge my dissertation supervisor Prof. Paulo Branco, for he's insights and guidelines that were an extreme contribute to this thesis.

On the other hand, this work is one more step on a long path, my academic journey, from my elementary school to my college I would like to thanks all teaching staff for giving me, step by step, the required tools to complete this work.

A big thanks to all my family and friends, who have accompanied me through this journey and allowed me good leisure and rest moments to continue working.

Finally, but the most important, a special thanks to my parents Jorge and Olga and my brother Rafael, for their unconditional support and without which this project would never be possible. For this and for guiding me and always wishing me the best, I'm truthfully gratefulness.

Abstract

Power cables, responsible for electric energy transmission, are subject to aging processes that continuously reduce the power cable capabilities to withstand the necessary efforts of its function, leading to eventual failure and an unpredictable power outage.

In this research, it is intended to study a methodology capable of detecting these phenomenons based on electric variables to detect faults and potential faults in low voltage lines.

For this, the influence of thermal aging and water trees in power cables insulators were studied, and simulations were developed based on the main changes discovered. The results of the various simulations were then compared through a process where most of the conductors' voltages are compressed into seven parameters.

This comparison showed that each of these phenomenons changed all seven parameters in different ways. In the case of the water trees, some of them were not detected. However, when discovered, it was possible to identify its location in the power cable.

Finally, it was made a flowchart that describes a process where the phenomenon suffered by the power cable is estimated based on the seven parameters, which in turn reflect the electric variables of its conductors.

Keywords

Power Cables; Thermal Aging; Water Trees; Simulation;

Resumo

Os cabos eléctricos, responsáveis pela transmissão de energia eléctrica, estão sujeitos a processos de envelhecimento que reduzem continuamente as capacidades dos cabos eléctricos para suportar os esforços necessários da sua função, levando a uma eventual falha e a um corte de energia imprevisível.

Com este trabalho, pretende-se desenvolver uma metodologia capaz de identificar os impactos destes fenómenos, tendo por base a análise de variáveis eléctricas, permitindo a detecção de falhas e de falhas potenciais em linhas de baixa tensão.

Para isso, foi estudada a influência do envelhecimento térmico e das *water trees* nos isolantes dos cabos, e de seguida foram realizadas simulações baseadas nas principais divergências descobertas. Os resultados obtidos das várias simulações foram então comparados através de um processo onde a tensão da maioria dos condutores do cabo foi comprimida em sete parâmetros.

Esta comparação mostrou que cada um destes fenómenos influencia o conjunto dos sete parâmetros de forma distinta. Para o caso das *water trees*, apesar de algumas não terem sido detectadas, quando o foram, foi possível determinar a sua localização no no cabo.

Por último, foi desenvolvido um fluxograma com o intuito de descrever um processo onde através da análise destes sete parâmetros, que reflectem as variáveis eléctricas dos condutores, se consegue estimar como o cabo foi afectado por estes fenómenos.

Palavras Chave

Cabos de energia; Envelhecimento Térmico; Water Trees; Simulações;

Contents

List of Figures

List of Tables

Nomenclature

ϵ	Electric Permittivity
ρ	Resistivity
σ	Electric Conductivity
D	Electric Displacement
d	Distance
E	Electric Field
F_e	Electrostatic Force
J	Current Density
k_c	Coulomb's constant
P	Power
Q	Volume's Charge
q	Electric Charge
T	Temperature
V	Electric Potential

Acronyms

XLPE Cross-linked polyethylene

PVC Polyvinyl chloride

FEMS Finite Element Method Software

WT Water Tree

FEM Finite Element Method

1

Introduction

Contents

The transmission of electrical energy requires an infrastructure to connect the producers to the consumers. One of the elements of this infrastructure is the power cables, which allow the connection between all the components of this system. Like every component, there's a constant deterioration due to its normal use and due to the environment where it is installed that reduces the ability to fulfil the initial requirements. This process is called *ageing*. When a power cable can no longer hold its purpose's efforts, there is an outage of energy transmission and it must be replaced.

1.1 Motivation

In the last years, with the increasing number of consumers and the development of micro-production with renewable energies, there was an increase in load and new profiles of consumption that provokes additional ageing of the power cables. As the detrition is stronger, the power outage becomes more frequent.

Beyond the increase of energy interruptions, there is a requirement for greater control of the power grid, which makes energy operators under huge pressure to reduce the downtime. So, there is a need to reduce the duration of interruptions. The solution can not be only the replacement of elements. It is necessary to identify faults and most important the incipient faults. For this, it is necessary a system that can identify faults and potential faults automatically and remotely without interfering with the power system, and it should also be able to be installed under already operating networks. A system with these characteristics would allow power operators to optimize the lifetime of power cables and plan the maintenance of infrastructures more efficiently, leading to a reduction of maintenance costs, reduction of component wasting and an increase of power system reliability.

1.2 State of the Art

When it comes to detect and locate power cable faults, there are already some equipment and techniques to do so. One example is the *thumping* method where a high voltage pulse is applied in one of the tips of the faulty cable. By doing so, this pulse will flow through the cable, and when it reaches a fault, it will provoke an electric arc and a loud noise that is used to locate the fault and the respective location. However, some studies on cables before and after this procedure shows that it damages the cable. [5] Another used method is based on the fact that a fault changes the propagation time of a pulse, which allows detecting the fault location with a precision of $\pm 5\%$. However, there's another problem associated with these two methods, they require the disassembly of the cable, which is very intrusive for the power grid.

There are also studies of a non-intrusive method to detect inception faults based on the wavelet

analysis. Inception faults, which may be proceeded by permanent faults, are phenomenons that produce a transient in electrical variables with a very short duration. The approach of this method is to identify a transient and recognise it as an inception fault, so a permanent fault can be expected in the future. [6]

1.3 Thesis Outline

This thesis proposes a different approach. It will analyse how the electric variables change with ageing of power cables and check for a pattern that can evince a potential fault. For this objective, this thesis will start with the electrostatics basis, in section 2.1, to study the natural behaviour of electric charges, and how the different environments influence its behave, and can be used to distinct purposes, conduct and sustain electric current. Then, in section 2.2, the limits of solid insulators to sustain the electrostatic forces were covered. There, the electronic configuration of an insulator is displayed, and the physical meaning of insulator's breakdown is discussed. Also, various ways to these phenomenons happens are included in this section.

After the electrostatics and the breakdown in solid insulators, this thesis continues with underground power cables, in section 2.3. Here, the structure of a power cable is displayed as well as the way some ageing phenomenons affect the power cable. The cable structure presented, is then used to define a reference 2D model, in chapter 3, where the methodology used to compare the results from the different simulations is also presented.

In chapter 4, the ageing phenomenons presented in section 5 are adapted to the reference model and then simulated.

To test the truthfulness of the 2D model simulations, especially for the *water trees*' simulations, chapter 5 has the definition of a 3D model. This model will be used to do similar simulations and to test the influence of *water trees*' size.

Finally, in chapter 6, the results from all simulations are analyzed to develop a methodology capable of estimate how the cable is being damaged based on electrical variables.

2

State of the Art

Contents

2.1 Electrostatics

According to Coulomb's Law, an electrostatic force F_e is defined as the existing force between two charged bodies at rest, and it is given by the equation (2.1).

$$\boldsymbol{F_{e_{12}}} = k_e \frac{q_1 q_2}{d_{12}^2} \hat{\boldsymbol{d_{12}}} \tag{2.1}$$

Where q_1 and q_2 represent the charge of body 1 and 2, respectively, d represents the distance between the two charges, and k_e represents Coulomb's constant which depends on the electric permittivity (ϵ) according to the equation (2.2).

$$k_e = \frac{1}{4\pi\epsilon} \tag{2.2}$$

On the other hand, knowing that the electric field (E) is defined as the force, per unit of charge, that an electric charge q_i would apply to a test charge q_t at the distance d_i, the electric force can also be defined in function of the electric field, as the equation (2.3) express.

$$\boldsymbol{F_{e_i}} = q_i \cdot \boldsymbol{E_i} \Leftrightarrow \tag{2.3}$$

$$\Leftrightarrow \boldsymbol{E_i} = \frac{1}{4\pi\epsilon} \frac{q_i}{d_i^2} \hat{\boldsymbol{d_i}} \tag{2.4}$$

This influence of multiple loads can be represented like figure 2.1.

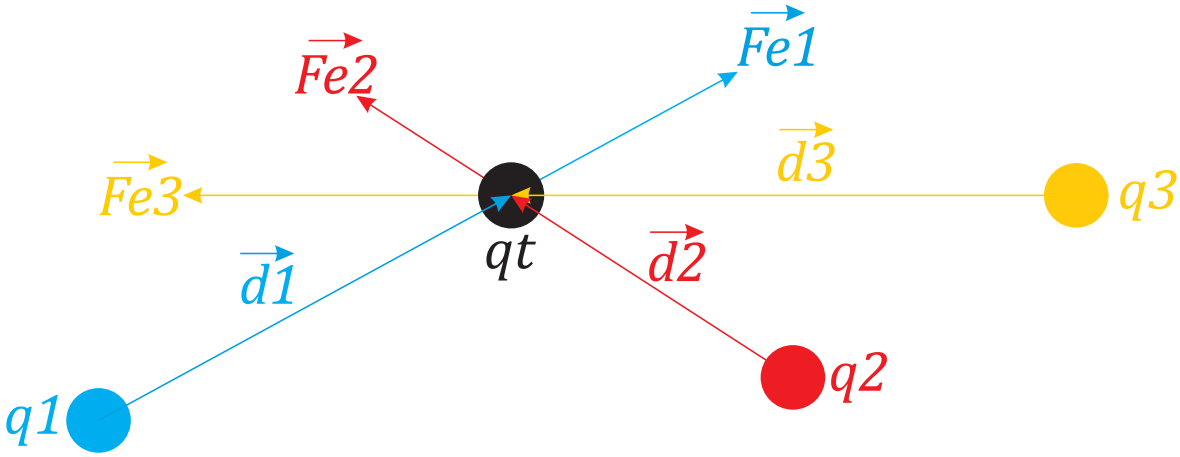

Figure 2.1: Influence of multiple loads in one hypothetical test charge

2.1.1 Electric Potential

As stated before, a test charge is a body that is not actually in the defined location. A test charge is a body that would be subject to certain forces if it would be placed in a specific point, and this is a potential.

Therefore, by Maxwell's equations for electrostatics conditions shown in expression (2.5),

$$\begin{cases} \nabla \times \boldsymbol{E} = 0 \\ \nabla \cdot \boldsymbol{D} = \rho \end{cases} \tag{2.5}$$

and with the mathematical condition that states that the curl of a gradient of a scalar function is always zero, it is possible to define the dependence of electric field of electric potential (V), which is expressed in equation (2.6) and equation (2.7), in the integral form [7].

$$\boldsymbol{E} = -\nabla V \tag{2.6}$$

$$V = -\int \boldsymbol{E} \cdot d\boldsymbol{l} \tag{2.7}$$

2.1.2 Electric Fields in Matter

Depending on the arrangement of the electron shell of an atom, specifically the gap between the valence band and conduction band, the charges can move more or less easily. Based on this property, it is possible to divide every material into two groups: electric conductor and insulator.

While in conductors the gap between the valence band and the conduction band is very short, allowing a free movement of the charges, in insulators only the cloud of electrons is displaced. [7]

2.1.2.A Conductor in an Electric Field

In conductors, when an electric field is applied, since the charges can move freely, they will move to the surface of the conductor, as represented in figure 2.2.

Since the charges will move to the surface of the conductor, the inside will become empty. So, if there are no charges in the interior of the conductor, the electric field will be null and the electric potential will be constant all over the conductor.

2.1.2.B Insulator in an Electric Field

For insulators, due to the lack of freedom of the charges, when an electric field is applied the charges will only move around atoms and will align with the electric field as figure 2.3 represents.

The level of alignment of the electric charges can be quantified through the electric displacement $(\boldsymbol{D})$, which relates to the electric permittivity and the electric field as expressed in equation (2.8).

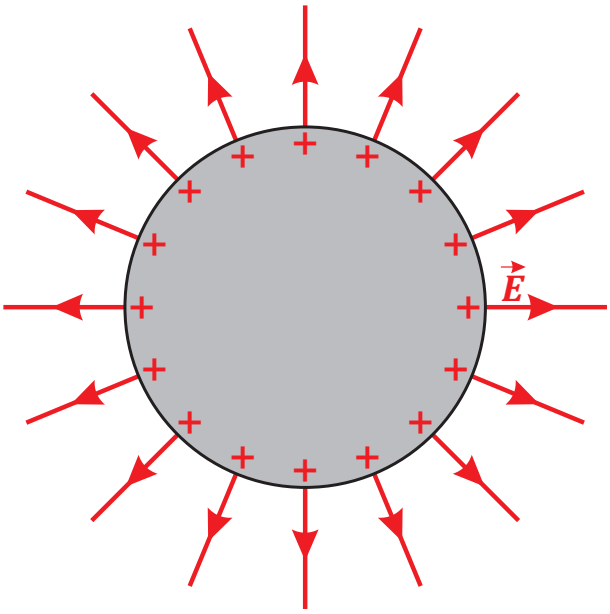

Figure 2.2: Charge distribution in a conductor when an electric field is applied

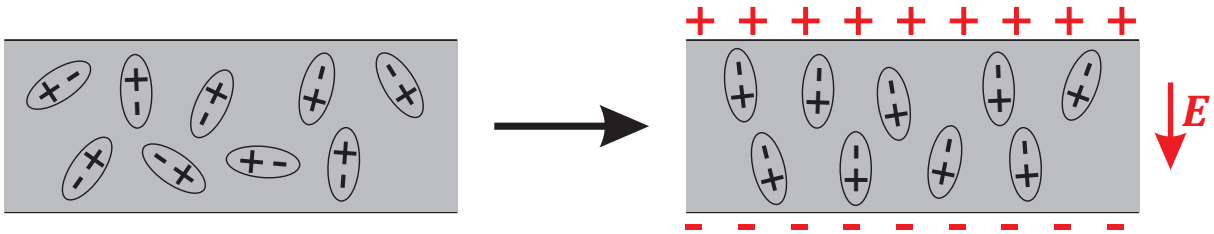

Figure 2.3: Charge distribution in an insulator

$$\boldsymbol{D} = \epsilon \boldsymbol{E} \tag{2.8}$$

On the other hand, and because there are charges in the interior of the insulator, the electric field is not zero and the electric potential is not constant.

2.2 Breakdown in Solid Insulation

As stated in section 2.1, an insulator also called a dielectric, is characterized by a big gap between the valence band and the conduction band. This interval, named bandgap (ΔW) and represented in figure 2.4, in normal situations, does not allow the electrons to move to the conduction band, making the number of holes and electrons in the same band very unbalanced and difficulting the electrons' flow.

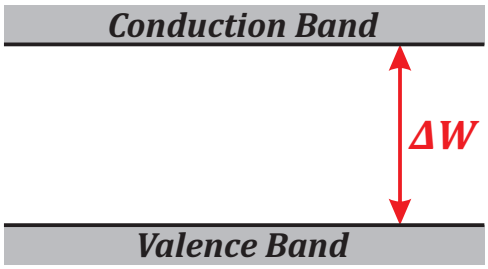

Figure 2.4: Electronic bands scheme

However, despite the high bandgap in dielectrics, in certain situations, electrons transition to the conduction band can occur to a level in which the dielectric can conduct electric currents. This phenomenon is called breakdown.

For solid dielectrics, the dielectric strength is higher when compared with gas and liquid dielectrics. However, solid dielectrics get permanently damaged when disruption occurs, while the gas fully and liquid partly recover when the applied electric field is extinct. [8].

The breakdown of solid dielectrics may occur in different ways. These are listed below and will be described in this chapter. They are:

- Intrinsic Breakdown
- Electromechanical Breakdown
- Thermal Breakdown
- Internal Discharges
- *Electrical Treeing* and *Water Treeing*

2.2.1 Intrinsic Breakdown

Ideally, the dielectrics don't have electrons in the conduction band. When it comes to reality, they exist, although in a very small amount. Real dielectrics also have some impurities that act as a trap for the electrons referred before, making the dielectric to maintain its insulator characteristics until certain limit values of the electric field. [8]

When that limit is crossed, there is the atoms' ionization leading to an increase of electrons than can no longer be trapped by the impurities, occurring the dielectric's intrinsic breakdown. The way these atoms are ionized divide this type of disruption into two categories: electronic breakdown and avalanche breakdown.

2.2.1.A Electronic Breakdown

The electronic breakdown is characterized by an initial high density of conduction electrons. Here, electrons from the valence band cross the bandgap and reach the conduction band by the influence of an external electric field. The repetition of this phenomenon increases the number of electrons in the conduction band and lead to a dielectric disruption. [8]

2.2.1.B Avalanche Breakdown

The avalanche breakdown in solid dielectrics is similar to disruption of gases. In this case, a free electron moving between two electrodes will collide with neutral molecules originating more free electrons. In turn, these new free electrons will ionize more molecules, leading to an avalanche of electrons from the cathode to anode, called *Townsend's Avalanches*, as figure 2.5 represents. [8]

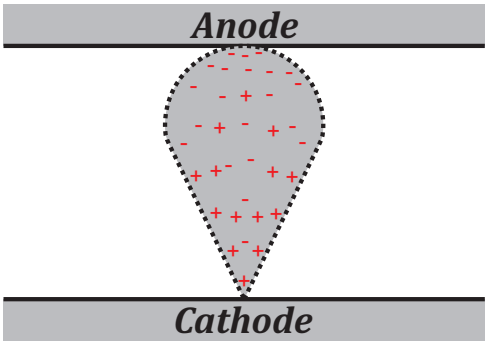

Figure 2.5: Townsend avalanches representation

2.2.2 Electromechanical Breakdown

Electromechanical breakdown occurs when the electric field applied to the dielectric gives origin to a mechanical stress that is higher than the limit it can support, called *dielectric strength*. Dielectric strength varies from material to material and is one of the main parameters when sizing an insulation system.

2.2.3 Thermal Breakdown

The current density (J) that flows through a dielectric is given by the expression (2.9), which can also be written like equation (2.10) if the electric field is sinusoidal. This current density can be decomposed into two components: conduction current density (J_c), which depends on the conductivity and the electric field, and displacement current density (J_d) that depends on the permittivity and the angular frequency.

$$\boldsymbol{J} = \sigma \boldsymbol{E} + \epsilon_r \epsilon_0 \frac{d\boldsymbol{E}}{dt} \tag{2.9}$$

$$\boldsymbol{J} = (\sigma + j\epsilon_r \epsilon_0 \omega)\boldsymbol{E} \tag{2.10}$$

Ideally, the conduction current density in a dielectric would be zero, however in real dielectrics, there is always a certain amount that causes joule losses leading to the heating of the dielectric. The power density of these losses is given by equation (2.11),

$$p_J = J_c E \Leftrightarrow p_J = \frac{1}{\rho(T)} E^2 \ [\mathrm{W\,m^{-3}}] \tag{2.11}$$

where $\rho(T)$ is the dielectric resistivity which depends on the temperature as (2.12) expresses,

$$\rho(T) = \rho_0 e^{-\gamma T} \ [\Omega\,\mathrm{m}] \tag{2.12}$$

where ρ_0 referrers to the resistivity of the dielectric determined at a specific temperature, and γ is a constant that satisfies the equation (2.12) for the experimental temperature. [9] So, assuming a uniform density, the joule losses will be the product of dielectric's volume with its joule density, as expressed in (2.13).

$$P_J = p_J V \ [\mathrm{W}] \tag{2.13}$$

Since the joule losses cause the heating of the dielectric, the temperature will only stabilize when joule losses (P_J) are equal to heat dissipation (P_d).

$$P_J(T) = P_d(T) \tag{2.14}$$

On its turn, the heat dissipation is proportional to the negative temperature gradient and the dielectric's surface area, according to Fourier's Law. Which, assuming again a uniform heat dissipation density, is given by (2.15),

$$P_d(T) = -AK\Delta T \ [\mathrm{W}] \tag{2.15}$$

where A is the dielectric's surface area, K is the material's thermal conductivity and ΔT is the temperature difference between the material and the environment. So expression (2.15) can be written as (2.16).

$$P_d(T) = AK(T - T_{environment}) \tag{2.16}$$

By sketching the expressions (2.11) and (2.16) in figure 2.6, it is possible to see that the equation (2.14) may have two solutions.

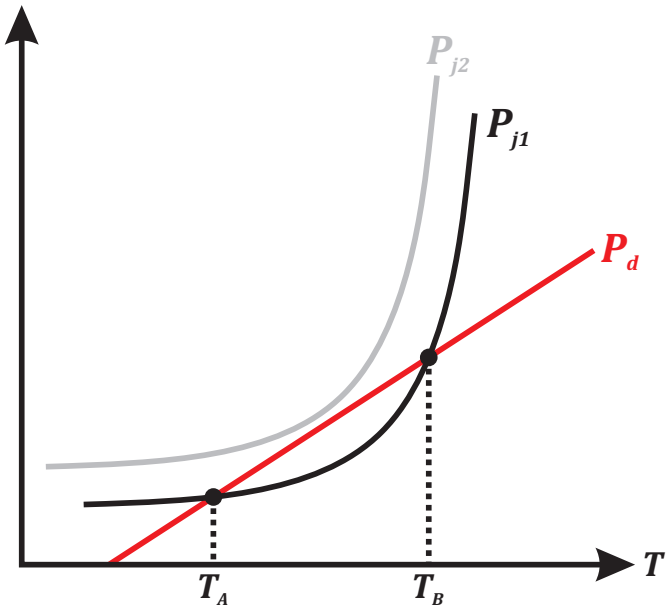

Figure 2.6: Evolution of Joule losses and heat dissipation with temperature

Although equation (2.14) may have two solutions for a certain electric field, it's possible to verify through figure 2.6 that one of them is unstable since the joule losses' derivative is higher than heat dissipation density derivative. This means that at this temperature, a minimum temperature variation may lead to dielectric's breakdown. So, to the dielectric's breakdown doesn't occur, the conditions in (2.17) must be satisfied.

$$\begin{cases} P_J(T) = P_d(T) \\ \frac{dP_J(T)}{dT} < \frac{dP_d(T)}{dT} \end{cases} \tag{2.17}$$

However, an increase of the electric field moves the joule losses line to the left. So, there's an electric field limit from which the conditions (2.17) can no longer be satisfied. The voltage that applies this electric field to the dielectric is called the *thermal breakdown voltage*.

2.2.4 Internal Discharges

Beyond the impurities, real dielectrics also have voids and cavities normally filled with air, which is a medium with lower electric permittivity and dielectric strength. [8]

In figure 2.7 there's a sketch of a dielectric cavity.

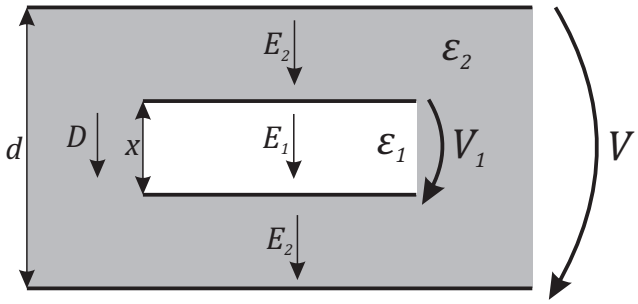

Figure 2.7: Dielectric's cavity schematic

Considering the figure's 2.7 geometry, if a voltage is applied to the terminals of the dielectric, there will be a uniform and constant electric displacement $(\vec{D})$ all over the insulator, including in the cavity. So, by equation (2.8), the relation between electric fields $\vec{E_1}$ and $\vec{E_2}$ expressed in (2.18) can be made.

$$\epsilon_1 \vec{E_1} = \epsilon_2 \vec{E_2} \Rightarrow \vec{E_2} = \frac{\epsilon_1}{\epsilon_2} \vec{E_1} \tag{2.18}$$

The electric displacement's uniformity also allows expressing the voltage V in the function of voltage V_1 and the electric field E_1 as in (2.19). By equation (2.18), this relation can be developed into (2.20).

$$V = V_1 + E_1(d - x) \tag{2.19}$$

$$V = V_1 \left(1 + \frac{\epsilon_1}{\epsilon_2} \frac{1}{x}(d - x)\right) \tag{2.20}$$

Let's assume a dielectric with relative permittivity $\epsilon_2 = 5.4$, a breakdown electric field $(E_{2_{break}})$ of $170\,\mathrm{kV\,cm^{-1}}$, a thickness (d) of $10\,\mathrm{mm}$ and one cavity filled with air with a thickness (x) of $1\,\mathrm{mm}$. If there was not a cavity, this dielectric would support, without any internal discharge, the voltage expressed in (2.21).

$$V = E_{2_{break}} d = 170\,\mathrm{kV} \tag{2.21}$$

However, to an internal discharge never happen, the electric field E_1 must not be higher than the air breakdown electric field $(E_{air_{break}})$, which is $30\,\mathrm{kV\,cm^{-1}}$. So, the maximum voltage that can be applied to the cavity is given by (2.22).

$$V_{1_{max}} = E_{air_{break}} x \Rightarrow V_{1_{max}} = 3\,\text{kV} \tag{2.22}$$

With this value, using equation (2.22) is possible to know what is the maximum voltage that can be applied to the dielectric without incurring any internal discharges.

$$V_{max} = V_{1_{max}} \left(1 + \frac{1}{\epsilon_R} \frac{1}{x}(d - x)\right) \Rightarrow V_{max} = 8\,\text{kV} \tag{2.23}$$

Despite the dielectric being sized to support a 170 kV voltage, there will be an internal discharge when the voltage applied is above 8 kV. This internal discharge consists of the generation of an electric arc that will annul the electric potential difference in the cavity. Once the electric potential difference is suppressed, the electric arc gets extinguished and the cavity's electric potential difference continues to follow (2.20). [8]

Individually, an internal discharge does not cause an insulation's breakdown. However, the multiple occurrences of this phenomenon cause an increase of the cavity's dimension, reducing the dielectric strength. This obtains importance when it's applied a periodical voltage with an amplitude above V_{max} since there will be an internal discharge at least in each period.

2.2.5 *Electrical Treeing* and *Water Treeing*

The presence of contamination in a dielectric's surface can work as a conductive film, and if there is an electric potential across the surface, there will be leakage currents. This contamination often is only moisture, however, the flow of leakage currents will heat and dry the surface causing the separation of the conductive film from the insulator. With this detachment, there will be a discontinuity that provokes an electric spark leading to the deterioration of the insulator's surface and the formation of conductive tracks through the dielectric. This event is called "tracking" and the expansion of channels in the form of branches, like figure 2.8, is called "treeing". [8] [10]

These trees can be divided into two groups: *Electrical Trees* and *Water Trees*.

2.2.5.A *Electrical Tree*

Electrical Trees are more visible and have a darker appearance. Since they're created by the erosion caused by electric sparks, carbonization is usually noticeable. On the other hand, this carbonization does not allow the appearance of the *electrical trees* to change as *water trees*.

Electrical Trees can also evolve from *Water Trees*, however, when this transition occurs, there's an imminent dielectric failure. [11]

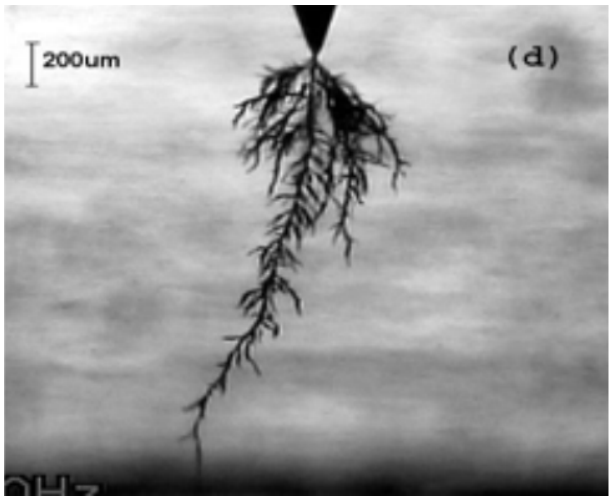

Figure 2.8: Tree (From *Electrical Treeing Characteristics in XLPE Power Cable Insulation in Frequency Range between 20 and 500 Hz* [1])

2.2.5.B *Water Tree*

A Water Tree (WT) have a diffuse appearance and their visibility depends on the dielectric's moisture [11], due to the process of WTs' formation. A WT is formed due to the deterioration caused when the dielectric is in contact with an ionic solution, and so they're strongly dependent on this kind of solution and considered a pre-breakdown process in the presence of moisture. [12]

In WTs, there are also two groups: the Bow-Tie *Water Trees* and the Vented *Water Trees*. While Bow-Tie WTs get started in a dielectric's interior fissure and, as they evolve, they expand in both directions. On the other hand, Vented WTs get started at the surface between the dielectric and an electrode and grows toward the other electrode. In figure 2.9 there's an example of a Vented WT and a Bow-Tie WT.

Figure 2.9: Vented Tree (Left) and Bow-Tie Tree (Right) (From *A Hybrid High Frequency Pulse and Pattern Recognition Method for Water Tree Detection in Long Distance Underground Cables* [2])

2.3 Underground Power Cables

2.3.1 Structure

Although there's a wide diversity of underground power cables, where the main changes are the number of conductors, nominal voltage and the thickness and type of insulator, there's also a structure in common between all of them. In figure 2.10, there's a representation of this structure, that will be abroad next.

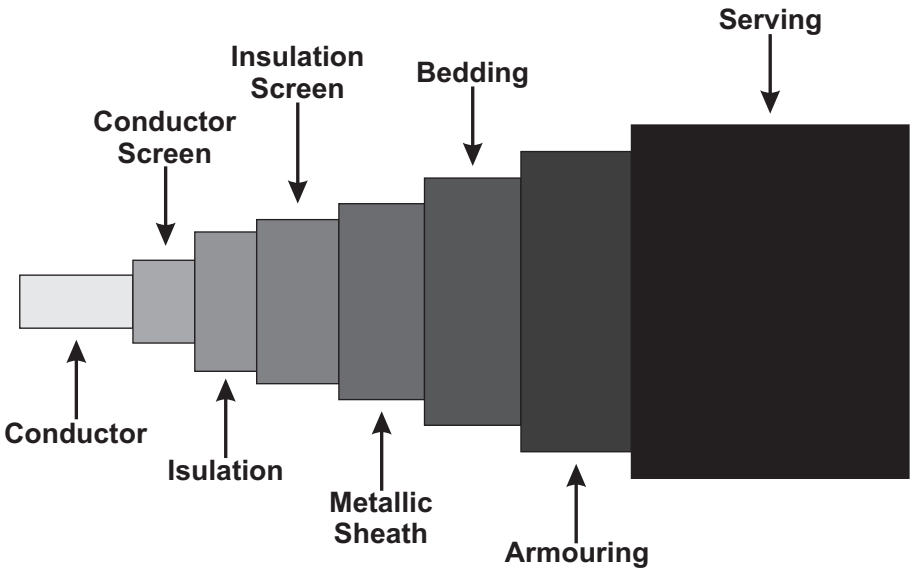

Figure 2.10: Underground power cables structure

2.3.1.A Conductor

Conductors are responsible for the transmission of electric energy, the main goal of a power cable. Thus, this component needs a high electrical conductivity to avoid a voltage drop between cable ends.

Also, some mechanical stresses need to be supported by conductors [13], so, to have the best balance between cost, electrical conductivity and mechanical strength, copper and aluminium are the most used materials for conductors.

On the other hand, the conductor's cross-section needs to be sized depending on the nominal power of the cable, since a larger cross-section reduces the resistivity and consequently the voltage drop.

2.3.1.B Insulator

Insulator's function is to avoid an electric current flux between the different conductors existing in the power cable. So, for having high dielectric strength, supporting high mechanical stresses, slow ageing,

and reduced maintenance costs, Cross-linked polyethylene (XLPE) is the dielectric preferred for power cables. [11]

It's thickness need to be adjusted in function of nominal voltage to avoid any dielectric breakdown or any other phenomenon specified in section 2.2.

2.3.1.C Screens

Generally, it's applied a semiconductor layer between the conductor and the insulator and the insulator and the sheath, in medium and high voltage power cables. This semiconductor aims to create an electric screen [13], which corresponds to minimize electrostatics forces by uniforming the electric field.

2.3.1.D Sheath

The sheath is a metallic layer evolving the insulator, usually composed of lead or aluminium. Its function is to protect the inner insulator and conductor from moisture and chemists that can exist in the surrounding environment.

2.3.1.E Bedding

The bedding is a layer of insulation material and as the function to protect the sheath from eventual damages caused by the armouring.

2.3.1.F Armouring

Armouring's function is to support most of the mechanical stress that the cable will suffer during its installation and operation. So, to accomplish this propose, armouring is generally built of steel.

2.3.1.G Serving

Serving is the final layer. Usually from an insulator material, like Polyvinyl chloride (PVC), its main objective is to protect the armouring from the exterior phenomenons.

2.3.2 Ageing

With the increase in the operation time, power cables' insulators lose their capacities until there's a permanent failure of the power cable. This degradation can occur in different ways, called ageing processes, which change the insulators' properties in different ways.

These properties variation can allow estimating the level of degradation of the power cable and, therefore, predict a potential failure.

2.3.2.A Thermal Ageing

A study has subjected XLPE samples to various temperatures during different periods and then has registered the evolution of properties of the samples [3]. One example is the evolution of relative permittivity of the insulator through the ageing time, where a replica is present in figure 2.11.

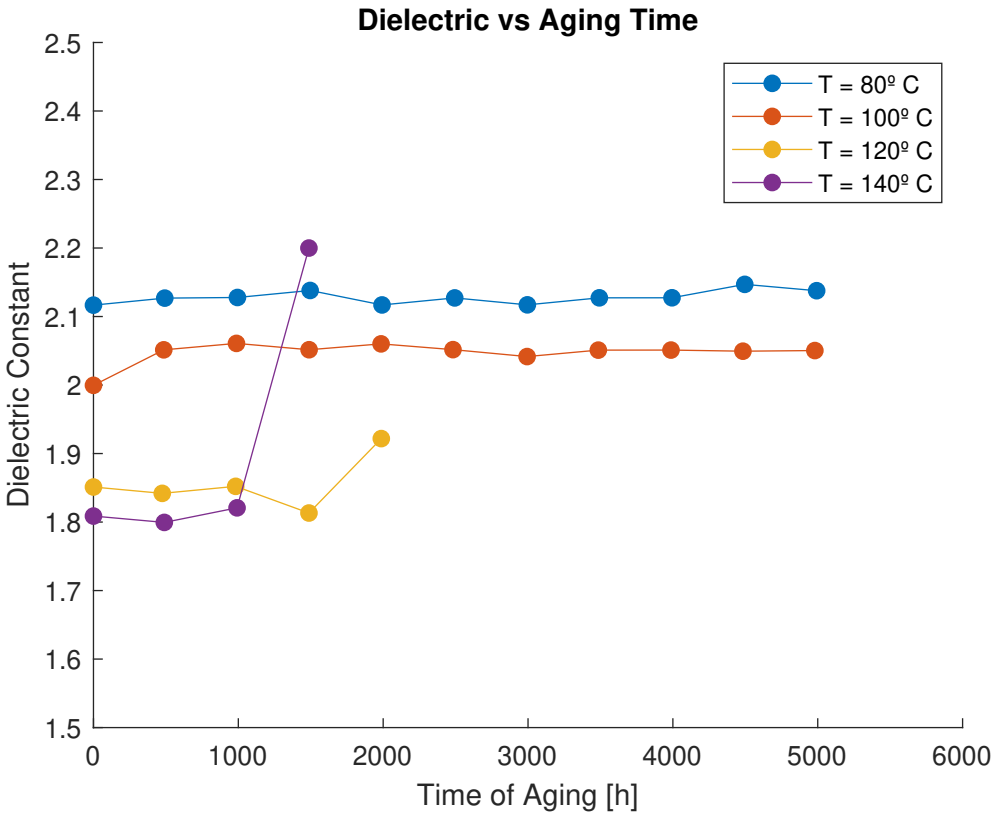

Figure 2.11: Relative permittivity evolution for ageing time (Adapted from *Dielectric and Mechanical Behavior of Cross-Linked Polyethylene Under Thermal Aging* [3])

The results show that for low temperatures, 80 °C and 100 °C, the relative electric permittivity variation is not significant, although there's a slight increase in the mean value. However, for high temperatures, 100 °C and 140 °C, there is a considerable increase of the relative electric permittivity after a specific ageing time. [3]

So, having in mind that a power cable operates at various temperatures during its life, its relative permittivity tends to increase with the operation time in real situations.

On the other hand, by analyzing the results in figure 2.11 at zero ageing time, it is visible that the relative permittivity tends to decrease with a temperature increase.

Therefore, in an overall situation, an increase in the relative permittivity may reflect the thermal ageing of the cable. A decrease of permittivity may indicate an increment of the temperature.

2.3.2.B *Water Trees*

As approached before in section 2.2.5.B, WT is a phenomenon that deteriorates the insulator over time, changing XLPE properties during it.

Another study [4] has exposed XLPE samples to sandblast to create the defects propitious to the formation of WT. This exposure had the goal to develop a uniform WT layer after an ageing process. The ageing process used consisted of the application of a $5\,\mathrm{kV}$ voltage at $10\,\mathrm{kHz}$ to the sandblasted XLPE samples, while dipped in a $NaCl$ solution. This process was then run for different periods, and the evolution of the damaged XLPE samples concerning time duration was registered. [4]

It allowed the plot of the relative permittivity of the damaged zone concerning ageing process time duration, replicated in figure 2.12.

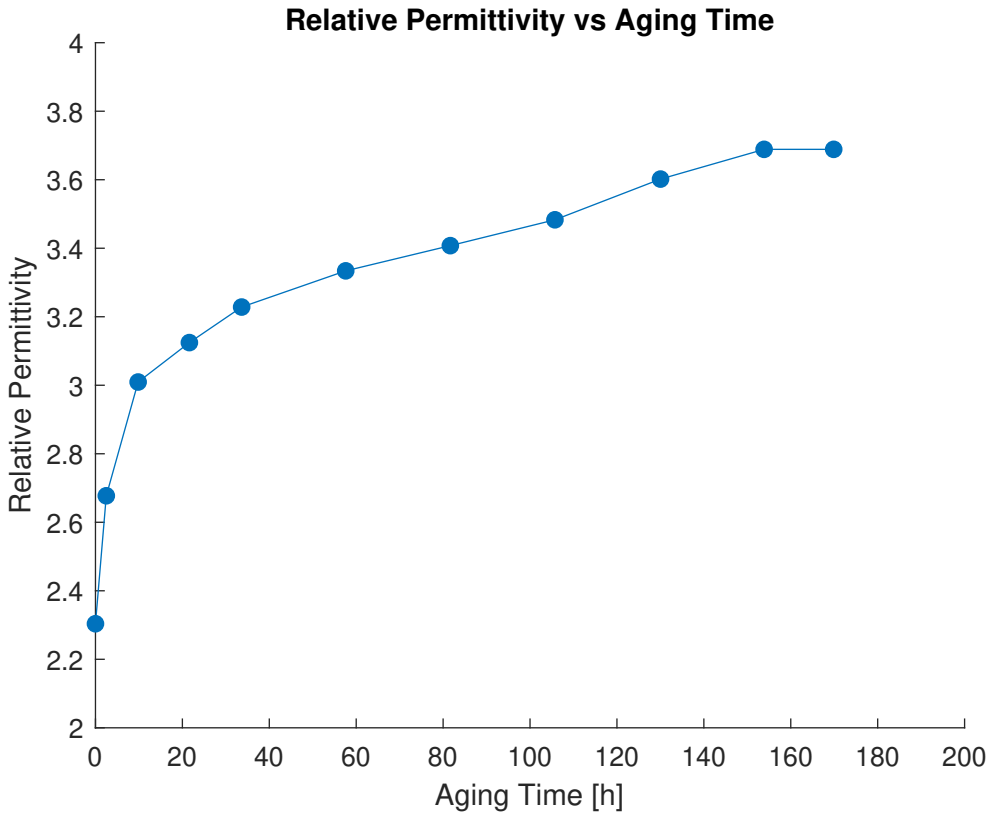

Figure 2.12: *Water Tree* relative permittivity evolution for ageing time (Adapted from *The Effect of Water Treeing on the Electric Field Distribution of XLPE* [4])

It's visible, from figure 2.12, that a WT causes a relative permittivity increase in the damaged area that can reach values over $60\,\%$ higher than a fresh XLPE sample.

3

Model Definition

Contents

3.1 Finite Element Method Software

As said in section 2.1, the electrostatics conditions are in equation (2.5), and by solving those equations, it is possible to determine the electric field and electric displacement vectors at any point.

Since a surface or a volume are groups of infinite points limited by certain constraints, by solving expression (2.5) conditions for all of these points it's possible to calculate the electric field and all associated variables all over a surface or a volume.

However, if there are infinite points, there will be infinite calculous, and this calculation will never end. That's where Finite Element Method (FEM) enters. FEM consists in the division of the surface or the volume into smaller parts, called finite elements. The interconnection between the boundaries of these elements define nodes which are the points where these calculations take place.

After the calculation of nodal points, the next step of FEM is to interpolate the solution of nodal points to the displaced points. This interpolation leads to accuracy loss, that is as lower as the higher is the number of nodal points, which corresponds to smaller elements.

Yet, a higher number of elements increase the computation time, which compel to the necessity to define a balance between accuracy and computation time is necessary.

Because of the tremendous number of calculous this method implies, this process is accomplished by a Finite Element Method Software (FEMS).

3.2 Power Cable Model

Based on the structure presented in section 2.3, and after some simplifications to reduce the computation time of simulations, the power cable shown in figure 3.1, was developed in a FEMS. It's dimensions and materials properties are also shown in expression (3.1) and table 3.1,respectively.

$$\begin{cases} R_c = 1.78\,\text{mm} \\ R_{ic} = 2.88\,\text{mm} \\ R_{bc} = 3.38\,\text{mm} \\ R_1 = 5.10\,\text{mm} \\ R_2 = 9.14\,\text{mm} \\ R_3 = 10.14\,\text{mm} \\ R_4 = 11.86\,\text{mm} \end{cases} \tag{3.1}$$

Table 3.1: Cable materials properties

	ϵ_r	σ [S m^{-1}]
Aluminium	1	3.5×10^7
Steel	1	1×10^7
XLPE	2.3	1×10^{-18}

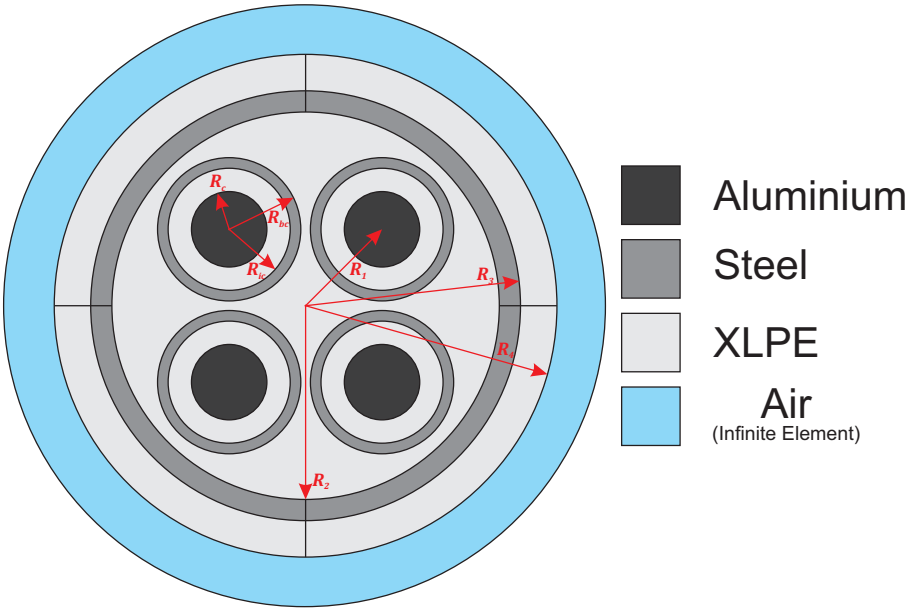

Figure 3.1: Cross section of an underground power cable model used in the 2D FEM study

By examining the power cable model, one verifies that, within phase conductors and sheaths, there are nine electric conductors that from now on will be identified as figure 3.2 represents. From these nine conductors, four of them (C_1, C_2, C_3 and C_N) will have imposed voltages, and the five sheaths (S_1, S_2, S_3, S_N and S_E) will have an electric potential dependent on the first four conductors and XLPE electrical properties.

3.3 Reference Simulation

Since the sheaths' electric potential depends on insulator's properties, its variation may manifest an insulator problem at an early stage. To study this possibility, a simulation of a reference model was first made. This simulation consists of the application of a pure sinusoidal three-phases and balanced system to the conductors C_1, C_2, C_3 and C_N, as defined in (3.2), to get the time evolution of all conductors' voltage.

$$\begin{cases} V_{C_1} = 230\sqrt{2}\cos\left(2\pi 50t\right) \\ V_{C_2} = 230\sqrt{2}\cos\left(2\pi 50t + \frac{2\pi}{3}\right) \\ V_{C_3} = 230\sqrt{2}\cos\left(2\pi 50t - \frac{2\pi}{3}\right) \\ V_{C_N} = 0 \end{cases} \quad [\text{V}] \tag{3.2}$$

It is relevant to state that, for this case, there is no harmonic or any noise in these electric potentials applied.

This time-dependent simulation gave as output the time evolution of three phase conductors' volt-

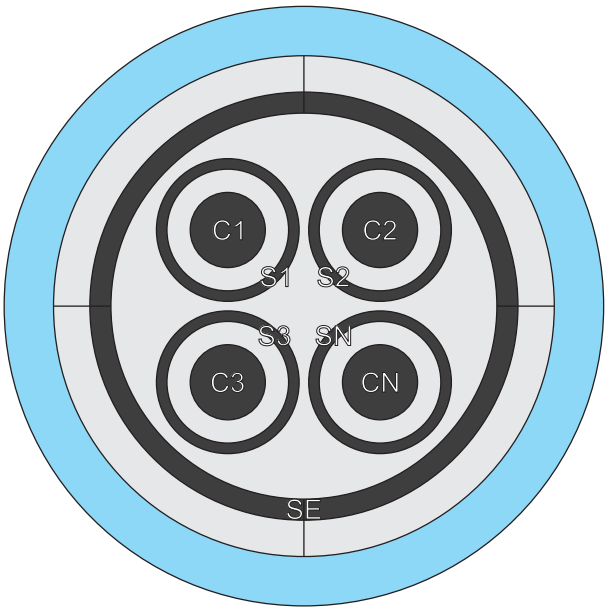

Figure 3.2: Conductors and sheaths identification

ages and the three respective sheaths' electric potentials. These voltages allow defining three electric potential difference signals expressed in (3.3), which will be used to plot the 3D graph in figure 3.3 and some of its perspectives, as shown in fig. 3.4(a) to 3.4(c).

$$\begin{cases} V_{\Delta 1} = V_{C_1} - V_{S_1} \\ V_{\Delta 2} = V_{C_2} - V_{S_2} \\ V_{\Delta 3} = V_{C_3} - V_{S_3} \end{cases} \tag{3.3}$$

The goal of electric potential difference definitions in equation (3.3) was to monitor the electric field between each conductor and respective sheath, thus any change in the insulator.

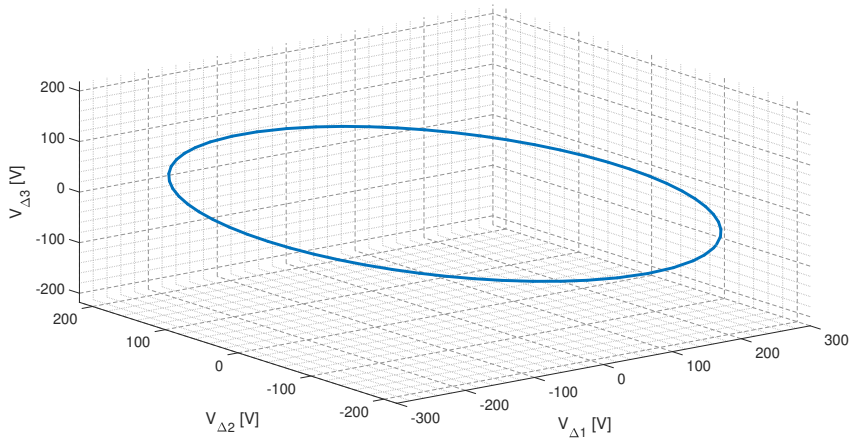

Figure 3.3: 3D pattern of V_{Δ} set of voltages obtained during a normal operating condition of the three-phase underground cable

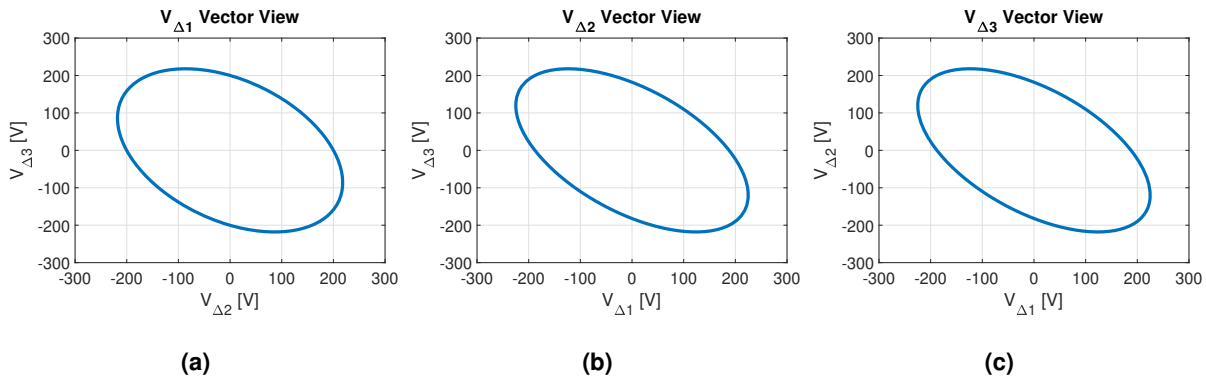

Figure 3.4: Reference 3D pattern of V_{Δ} set of voltages view from: **a)** $V_{\Delta 1}$ perspective; **b)** $V_{\Delta 2}$ perspective; **c)** $V_{\Delta 3}$ perspective

From figures 3.3 and 3.4, it's visible that the plot of these voltages defines a pattern described by an ellipse inserted in an arbitrary 3D plane. So, the 3D representation in fig. 3.3 can be simplified by looking to the 3D ellipse from the normal perspective to its plane. To do this, it is required to determine the plane's equation where the 3D ellipse is contained by adjusting equation expressed in (3.4) to the ellipse points.

$$Ax + By + Cz + D = 0 \tag{3.4}$$

After having the plane equation, the normal vector $(\vec{n})$ is given by (3.5) and represented in figure 3.5.

$$\vec{n} = (A, B, C) \tag{3.5}$$

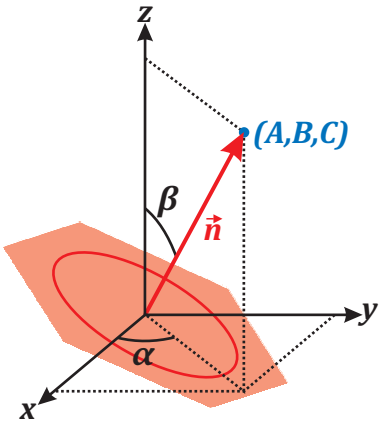

Figure 3.5: Normal vector representation

Now, to simplify the representation of this pattern, the ellipse's plane must be transformed so that it becomes parallel to the XY plane, which is equivalent to align the normal with the Z vector. This

transformation can be decomposed into two elementary rotations.

3.3.1 Transformation 1

This transformation is the rotation of the normal vector around $\boldsymbol{Z}$ with an amplitude of $-\alpha$, where α is normal's azimuth that is represented in figure 3.5 and can be calculated through equation (3.6).

$$\alpha = \arctan\left(\frac{B}{A}\right) \tag{3.6}$$

Transformation 1 is analytically defined as matrix T_1, replicated in equation (3.7).

$$T_1 = \begin{bmatrix} \cos\alpha & \sin\alpha & 0 \\ -\sin\alpha & \cos\alpha & 0 \\ 0 & 0 & 1 \end{bmatrix} \tag{3.7}$$

3.3.2 Transformation 2

This transformation is the rotation of the normal vector around $\boldsymbol{Y}$ with an amplitude of $-\beta$, where β is the altitude angle of the normal, also represented in figure 3.5, that can be calculated through equation (3.8).

$$\beta = \arctan\left(\frac{\sqrt{A^2 + B^2}}{C}\right) \tag{3.8}$$

Transformation 2 is analytically defined as matrix T_2, replicated in equation (3.9).

$$T_2 = \begin{bmatrix} \cos\beta & 0 & -\sin\beta \\ 0 & 1 & 0 \\ \sin\beta & 0 & \cos\beta \end{bmatrix} \tag{3.9}$$

Once the two transformations are defined, the new coordinates will be given by expression (3.10).

$$\begin{bmatrix} x' \\ y' \\ z' \end{bmatrix} = T_1 T_2 \begin{bmatrix} x \\ y \\ z \end{bmatrix} \tag{3.10}$$

These new coordinates will represent the pattern in such a way that its plane will be parallel with the XY plane. So, the ellipse can be described in a 2D graph instead of a 3D as before.

When it comes to analyzing an ellipse in a two-dimensional space, it is characterized by five parameters that are listed below and sketched in figure 3.6.

- $\boldsymbol{a}$ - Longest axis length
- $\boldsymbol{b}$ - Shortest axis length

- x_0 - x coordinate of ellipse's center
- y_0 - y coordinate of ellipse's center
- θ - Longest axis slope

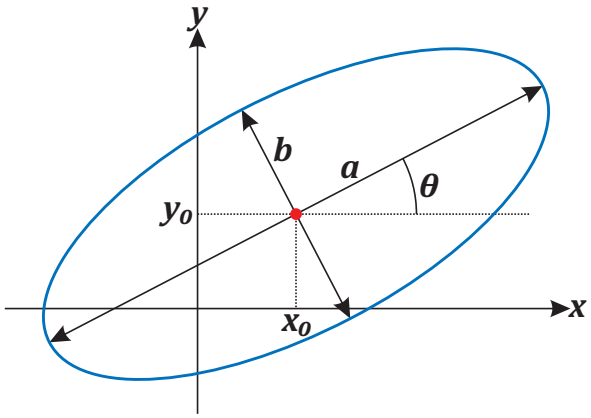

Figure 3.6: Ellipse parameters

An ellipse can also be described analytically through the equation (3.11), which can be fitted to the new coordinates point's of the ellipse's, as was done to plane's equation. The relation between this equation's constants and the parameters defined above are also specified in equations (3.12) to (3.15).

$$Ex^2 + Fxy + Gy^2 + Hx + Iy + J = 0 \tag{3.11}$$

$$a, b = \frac{-\sqrt{2\left(EI^2 + GH^2 - FHI + (F^2 - 4EG)J\right)\left((E+G) \pm \sqrt{(E-G)^2 + F^2}\right)}}{F^2 - 4EG} \tag{3.12}$$

$$x_0 = \frac{2GH - FI}{F^2 - 4EG} \tag{3.13}$$

$$y_0 = \frac{2EI - FH}{F^2 - 4EG} \tag{3.14}$$

$$\theta = \begin{cases} \arctan\left(\frac{1}{F}(G - E - \sqrt{(E-G)^2 + F^2})\right), & B \neq 0 \\ 0° & B = 0, E < G \\ 90° & B = 0, E > G \end{cases} \tag{3.15}$$

With these variables, the pattern in figure 3.3 is reduced to seven parameters: α, β, a, b, x_0, y_0 and θ. For the reference simulation, these parameters results are presented in Table 3.2. This values will

be compared with other simulations and analyzed to detect some changes that may occur in the cable's insulator.

Table 3.2: Reference simulation results

$\boldsymbol{\alpha}$ [°]	$\boldsymbol{\beta}$ [°]	$\boldsymbol{a}$ [V]	$\boldsymbol{b}$ [V]	$\boldsymbol{x_0}$ [V]	$\boldsymbol{y_0}$ [V]	$\boldsymbol{\theta}$ [°]
43.19	55.61	281.67	257.54	0.03	0.02	−58.98

4

Simulations

Contents

4.1 Thermal Ageing Simulation

Based on the XLPE behaviour due to thermal ageing, presented in section 2.3.2.A, simulations in a FEMS were developed to analyze the outcome of insulator's thermal ageing.

Since the phase conductors are the main thermal source in a power cable [14], the XLPE's local average temperature will be higher as the closer it is from the phase conductors. So, having in mind the study [3], presented in section 2.3.2.A, these regions will manifest changes earlier. So, this simulation study will divide the model's XLPE domain into two groups, as figure 4.1 shows. Group 1 is formed by the XLPE's regions furthest from the phase conductors where the relative electric permittivity (ϵ_1) is fixed to 2.1. Group 2 is composed of the domains nearest from these conductors and the relative electric permittivity of this group (ϵ_2) will be changed due thermal ageing.

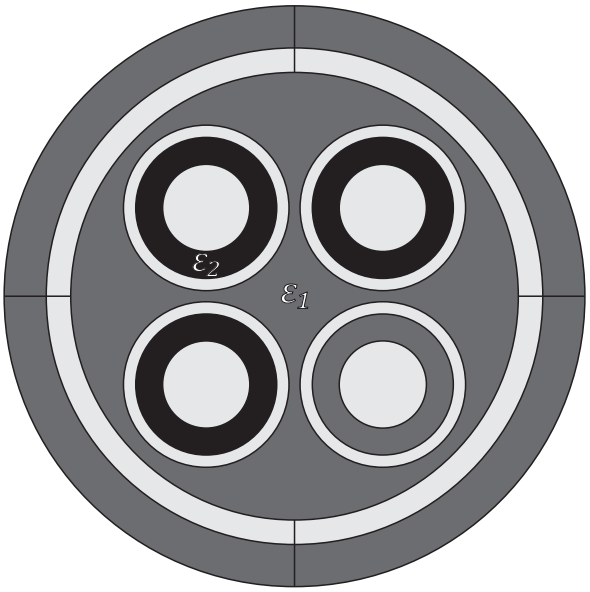

Figure 4.1: XLPE's domain division

To the phase conductors, it was applied a pure sinusoidal three-phase balanced system, as defined in equation (3.2).

After the simulations were completed, the outputs were processed as described in chapter 3, leading to the results presented in Table 4.1. From table 4.1, the case where ϵ_2 is 2.1 corresponds to the situation where the relative electric permittivity in group 1 is equal to the one in group 2. This scenario represents uniform thermal age and temperature all over the XLPE's domain, which probably coincides with an unaged cable at rest. So, the deviations from the other situations to this one were calculated. These divergences are displayed in percentage in Table 4.2. And its evolution with the permittivity difference, between group 1 and group 2, are plotted in figures 4.3(a) to 4.3(g). If this difference is higher than zero, the permittivity of group 2 is higher than group 1, which indicates the nearest regions are more degraded

or at a lower temperature. On the other hand, if the difference is lower than zero, the permittivity of group 2 is lower than group 1, indicating a higher temperature in these regions.

Table 4.1: Thermal ageing simulation results

ϵ_2	α[°]	β[°]	a[V]	b[V]	x_0[V]	y_0[V]	θ[°]
1.8	43.24	55.59	293.5	270.82	−0.08	0.13	−59.17
1.95	43.21	55.6	287.23	263.82	−0.09	0.12	−59.14
2.1	43.19	55.61	281.24	257.15	−0.09	0.12	−59.12
2.3	43.16	55.63	273.63	248.77	−0.07	0.11	−59.1
2.5	43.14	55.64	266.4	240.92	−0.09	0.1	−59.08
2.8	43.11	55.65	256.25	230.05	−0.08	0.09	−59.06
3	43.09	55.66	249.92	223.31	−0.12	0.08	−59.03
3.2	43.07	55.67	243.88	216.97	−0.07	0.12	−59.02
3.5	43.05	55.68	235.36	208.1	−0.05	0.11	−58.99
3.7	43.04	55.68	230	202.59	−0.07	0.1	−59

Table 4.2: Thermal ageing deviation results

$\epsilon_2 - \epsilon_1$	α[%]	β[%]	a[%]	b[%]	x_0[%]	y_0[%]	θ[%]
−0.3	0.12	−0.05	4.36	5.32	−16.74	8.52	0.08
−0.15	0.06	−0.02	2.13	2.59	3.23	6.55	0.03
0	0	0	0	0	0	0	0
0.2	−0.07	0.02	−2.71	−3.26	−25.14	−5.81	−0.03
0.4	−0.12	0.05	−5.28	−6.31	−1.32	−14.08	−0.07
0.7	−0.19	0.07	−8.88	−10.54	−7.63	−22.34	−0.1
0.9	−0.24	0.09	−11.14	−13.16	36.21	−33.6	−0.15
1.1	−0.27	0.1	−13.28	−15.62	−21.01	1.89	−0.17
1.4	−0.32	0.12	−16.31	−19.07	−40.46	−3.0	−0.21
1.6	−0.34	0.13	−18.22	−21.22	−26.08	−17.16	−0.2

Figure 4.2 graphs show that the XLPE's increase of the electric permittivity in the regions nearest to phase conductors causes changes in the pattern defined before. Although x_0 and y_0 variables do not seem to have a relation with the electric permittivity, beta increases, and alpha, a, b and θ decrease with the raise of this property. These variations are in the order of $+20\,\%$ for a and b and $0.25\,\%$ for α, β and θ when permittivity increase from 2.1 to 3.7.

However, as stated before, for this case, the increment in electric permittivity can have two causes: XLPE's thermal ageing or a reduction in the insulator temperature due to possible external causes. So, since the main goal is to estimate the age of the power cable, it is necessary to distinguish the cause. Since the thermal ageing is an irreversible phenomenon unlike temperature changes, when a and b reach values never reached, this should indicate a raise in thermal age.

However, besides this methodology would only estimate the temperature difference between group 1 and 2 with poor accuracy, it would also assume there was not an external influence. So, having temperature data about the conductors and the cable environment would allow a better method for this task. This way it was possible to check if there was a temperature change and detect its origin, and,

finally distinguish the cause of an increase of the electric permittivity: the thermal ageing or a reduction in temperature.

In case there as a decrement in electric permittivity difference, that could only represent a temperature increase of the conductors. Again, with temperature data, that was possible to double-check this hypothesis, which would increase the accuracy.

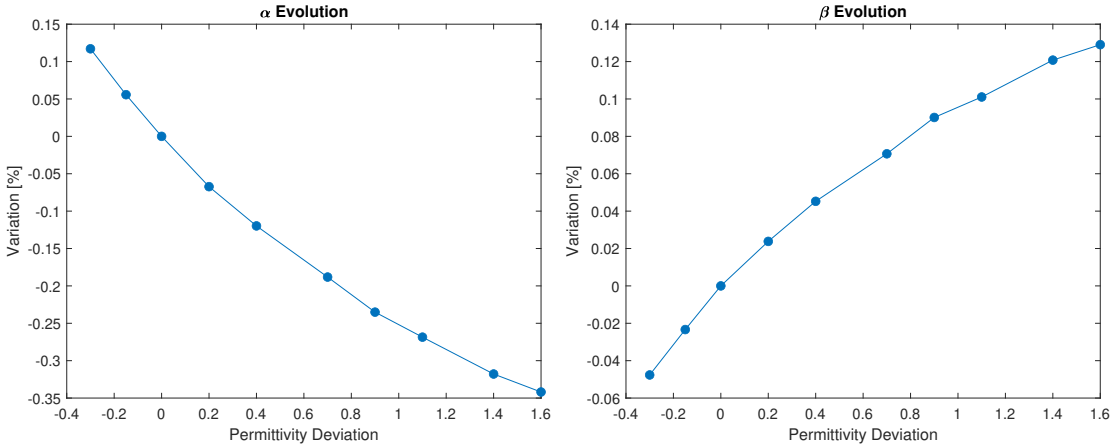

(a) Evolution of α **(b)** Evolution of β

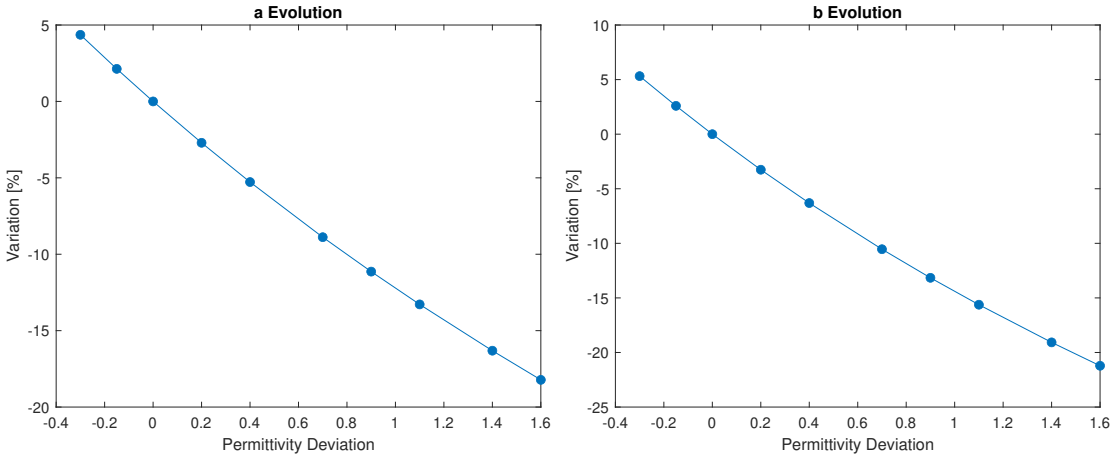

(c) Evolution of a **(d)** Evolution of b

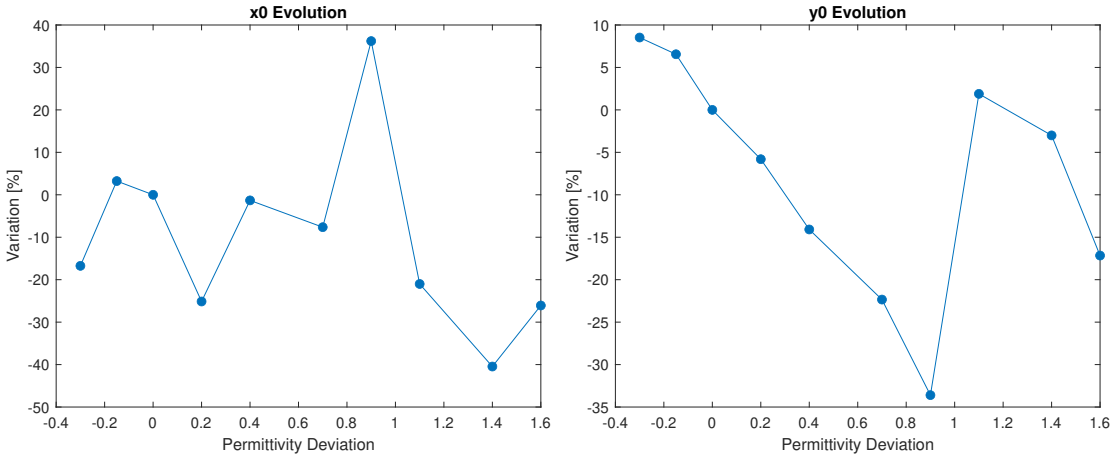

(e) Evolution of x_0

(f) Evolution of y_0

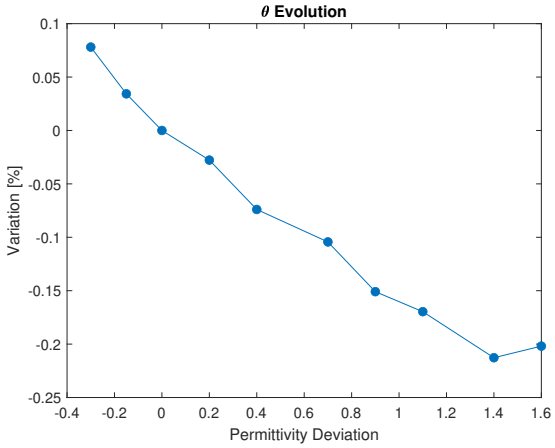

(g) Evolution of θ

Figure 4.2: Ellipse parameters evolution with the relative electric permittivity difference.

4.2 *Water Trees* Simulation

Since WTs are a very typical phenomenon in power cables and are considered a pre-breakdown process in the presence of moisture [12], FEM simulations have been run to analyze if its formation can be detected.

As referred before, in section 2.2.5.B, WTs are divided into two groups: the Vented WTs and the Bow-Tie WTs. However, the Vented WTs are considered more threatening [12], so all simulations are focused on this type. This option, allows restricting the location of WT's root to the unbundling surfaces of the insulator.

As shown in figure 4.3, multiple semi-ellipses, representing a damaged region due to a Vented WT, were defined. These semi-ellipses are characterized by a semi-axis length of $0.25\,\mathrm{mm}$ and $0.6\,\mathrm{mm}$.

Since it is expected that greater proximity between a WT and a phase conductor provokes a higher variation in electric variables, three critical groups were defined:

- **Critical Group I:** Includes the locations were the WTs' roots are closer to a phase conductor. ($-135°$ and $-225°$)
- **Critical Group II:** Is composed of intermediate locations where the WTs' roots have a phase conductor which is closer to them. ($-112.5°$, $-157.5°$, $-202.5°$ and $-247.5°$)
- **Critical Group III:** This group includes the locations further from the conductors, which have two conductors at the same distance. ($-90°$,$-180°$ and $-270°$)

Having in mind that the neutral conductor will have a null voltage, the electric field around this conductor is lower than the other regions. On the other hand, the phase conductor 2's adjacent conductors is a phase and the neutral conductor, just like the case of phase conductor 3. So, simulations were only made in locations in $-90°$ to $-270°$ range.

For each of those locations in figure 4.3, two simulations have been run: one where semi-ellipse domain relative electric permittivity is 3.0 and the other where it is 3.7. These values represent the the severity stage of the WT, as covered in section 2.3.2.

From the simulations' outputs, the seven pattern parameters established in chapter 3 were calculated and are present in tables 4.3 and 4.4 for the relative electric permittivity of 3.0 and 3.7, respectively. For both tables, on the left side, it is the WT location and its respective critical group, followed by the absolute values of the seven pattern's parameters calculated, in the right side.

After the first look at tables 4.3 and 4.4, it's visible that the amplitude of variations is much lower than the range of the values. So, identical tables, where the results are expressed as the percentage of the deviation from the reference values established in chapter 3, were developed and are presented in tables 4.5 and 4.6, for the relative electric permittivity of 3.0 and 3.7, respectively.

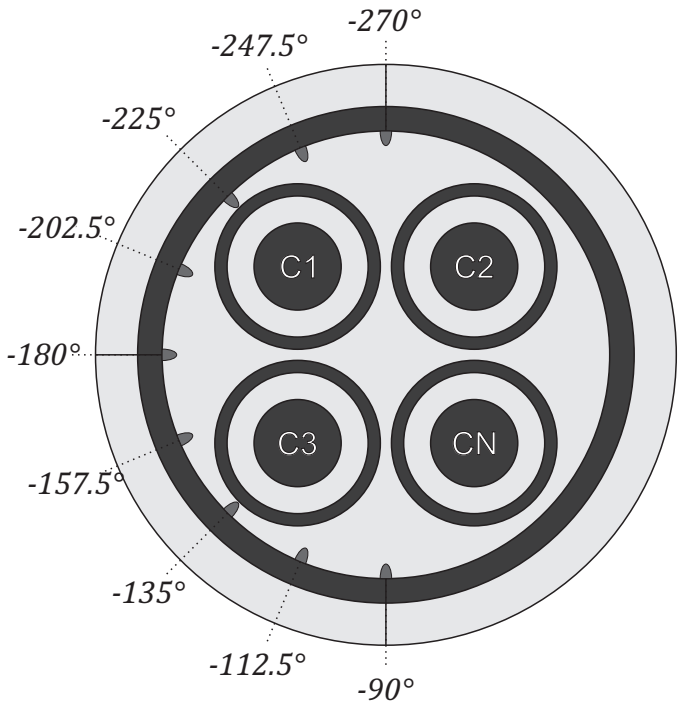

Figure 4.3: *Water trees* locations

The results from tables 4.5 and 4.6 shows some oscillations over all locations. However, for areas from the critical group I, there are higher variations. To visualize these details and to compare the results from these two tables, the evolution of each parameter along with WT's location was plotted in figure 4.4.

To better link the x-axis of the graphs in figure 4.4 with the WT location, vertical auxiliary dotted lines were added. For example, the vertical auxiliary line denoted as *"Phase 3"* matches the place in figure 4.3 where the WT is closer to the conductor C_3, this is at $-135°$. On the other hand, the case with vertical auxiliary line denoted as *"Phase 1 - Phase 3"* is for the middle area between conductors C_1 and C_3, at $-180°$.

Figure 4.4 graphs show that the ellipse parameters variation is very low, less than $1\,\%$ for almost every variable. However, some variations peaks reveal a certain degree of confidence to detect the existence of a WT.

Parameter α, in figure 4.5(a), has some fluctuations around 0 with an amplitude approximately $0.1\,\%$, but, for the case where the WT is closer to the phase 3, there's a $0.4\,\%$ peak, four times higher than this fluctuation.

In figure 4.5(b), parameter β has similar behaviour to α, an oscillation of $0.04\,\%$ around 0 and a $0.125\,\%$ spike also at $-135°$.

When examining ellipse's dimensions, variables a and b, there are no oscillations, only a $0.19\,\%$ peak

Table 4.3: *Water trees* simulation results when having an average relative electric permittivity of 3.0

$Location[°]$	Critical Group	$\alpha[°]$	$\beta[°]$	a[V]	b[V]	x_0[V]	y_0[V]	$\theta[°]$
-90	III	43.18	55.62	281.66	257.55	0.11	0.05	-58.96
-112.5	II	43.22	55.61	281.69	257.56	-0.14	0.01	-58.84
-135	I	43.34	55.65	281.7	258.06	-0.47	0.05	-58.73
-157.5	II	43.12	55.63	281.72	257.54	-0.23	0.03	-58.81
-180	III	43.2	55.59	281.66	257.55	-0.01	-0.01	-58.95
-202.5	II	43.2	55.62	281.66	257.55	-0.1	0.03	-58.94
-225	I	43.22	55.63	281.94	257.54	0.17	-0.25	-59.01
-247.5	II	43.18	55.6	281.7	257.53	0.04	0.02	-58.93
-270	III	43.13	55.61	281.65	257.55	-0.08	0.03	-58.91

Table 4.4: *Water trees* simulation results when having an average relative electric permittivity of 3.7

$Location[°]$	Critical Group	$\alpha[°]$	$\beta[°]$	a[V]	b[V]	x_0[V]	y_0[V]	$\theta[°]$
-90	III	43.16	55.61	281.66	257.56	0.04	0.05	-58.94
-112.5	II	43.2	55.62	281.68	257.64	-0.25	0.03	-58.83
-135	I	43.33	55.68	281.76	258.29	-0.19	0	-58.46
-157.5	II	43.17	55.62	281.65	257.63	0.08	0	-58.9
-180	III	43.17	55.61	281.66	257.53	-0.02	0.03	-58.91
-202.5	II	43.19	55.61	281.71	257.53	0.05	-0.01	-58.92
-225	I	43.22	55.59	282.2	257.54	0.21	-0.18	-58.99
-247.5	II	43.19	55.61	281.77	257.54	-0.08	0.07	-58.84
-270	III	43.14	55.61	281.66	257.55	0	-0.01	-58.92

at $-225°$ in parameter a, and $0.3\,\%$ at $-135°$ in variable b. There is also a rise of $0.03\,\%$ in a when the WT is closer to phase 3 that, since it doesn't seem reliable, it will be despised.

For the ellipse's centre, in figures 4.5(e) and 4.5(f), there's only a considerable change in y_0 to refer, also only when the WT is nearer the phase 1.

Finally, θ's deviation has a fluctuation around 0 too, but, for this case, the variation is in the order of $0.2\,\%$. θ also has a higher change, about $0.9\,\%$, when the WT is located at $-135°$.

In an overall view, although it was possible to identify the affected phase, only the WT located in the regions nearest to phase conductors sheats. However, as said before, WTs grow in an electrode direction, which means that, as they evolve, they become closer to these conductors and could be detected, although in a more advanced stage.

Table 4.5: *Water trees* deviation results from reference to an average relative electric permittivity of 3.0

$Location[°]$	Critical Group	$\alpha[\%]$	$\beta[\%]$	$a[\%]$	$b[\%]$	$x_0[\%]$	$y_0[\%]$	$\theta[\%]$
-90	III	-0.02	0.02	0	0.01	238.92	230.11	-0.03
-112.5	II	0.07	-0.01	0.01	0.01	-535.19	-15.64	-0.25
-135	I	0.35	0.07	0.01	0.2	-1568.33	259.24	-0.42
-157.5	II	-0.16	0.03	0.02	0	-802.65	98.44	-0.29
-180	III	0.03	-0.05	0	0	-130.27	-144.97	-0.06
-202.5	II	0.01	0.02	0	0	-401.36	125.74	-0.07
-225	I	0.08	0.04	0.1	0	427.72	-1764.13	0.05
-247.5	II	-0.02	-0.02	0.01	0	39.51	24.99	-0.09
-270	III	-0.13	-0.01	-0.01	0.01	-335.57	65.52	-0.12

Table 4.6: *Water trees* deviation results from reference to an average relative electric permittivity of 3.7

$Location[°]$	Critical Group	$\alpha[\%]$	$\beta[\%]$	$a[\%]$	$b[\%]$	$x_0[\%]$	$y_0[\%]$	$\theta[\%]$
-90	III	-0.07	0	0	0.01	26.17	202.11	-0.06
-112.5	II	0.01	0.01	0	0.04	-864.79	111.6	-0.25
-135	I	0.32	0.12	0.03	0.29	-697.37	-110.12	-0.88
-157.5	II	-0.04	0	-0.01	0.04	144.46	-93.59	-0.14
-180	III	-0.05	0	0	0	-173.14	96.15	-0.12
-202.5	II	0.01	-0.01	0.01	0	61.34	-136.81	-0.11
-225	I	0.07	-0.04	0.19	0	564.57	-1310.98	0.01
-247.5	II	0.01	-0.01	0.03	0	-333.12	384.33	-0.24
-270	III	-0.13	0	0	0.01	-95.44	-164.89	-0.1

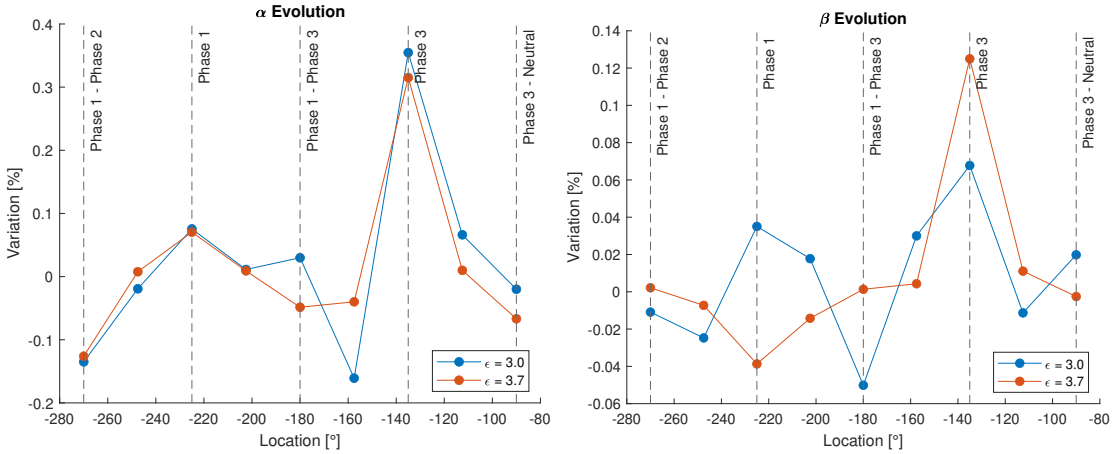

(a) Evolution of α

(b) Evolution of β

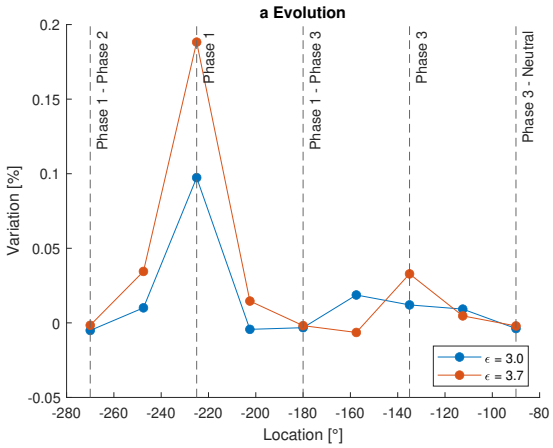

(c) Evolution of a

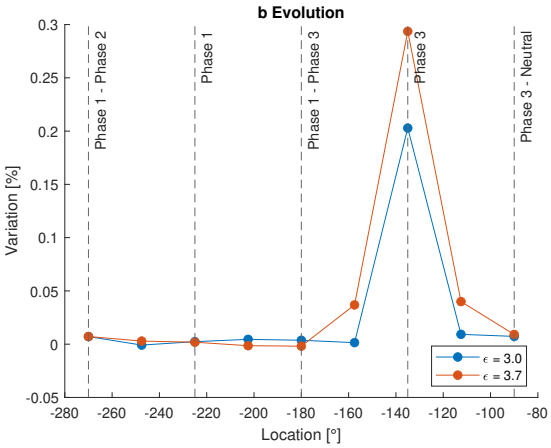

(d) Evolution of b

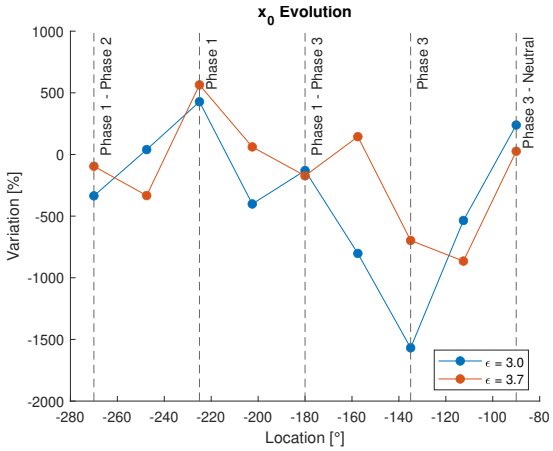

(e) Evolution of x_0

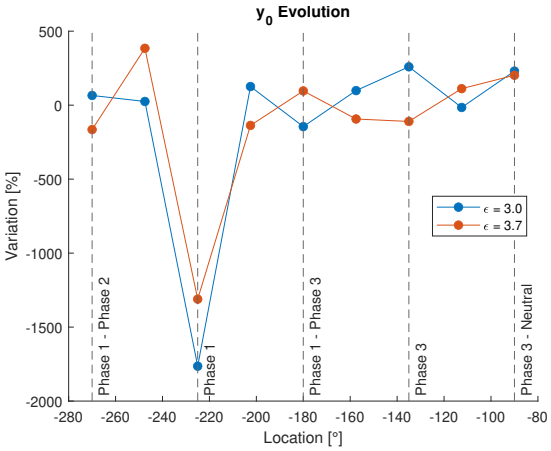

(f) Evolution of y_0

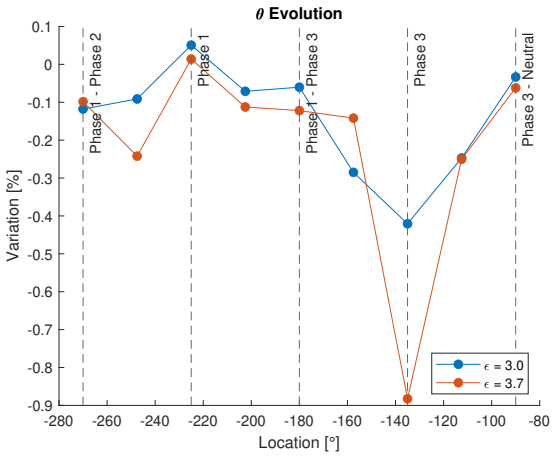

(g) Evolution of θ

Figure 4.4: Ellipse parameters evolution along with *water tree* location

5

3D FEM Model's Simulations

Contents

In chapter 4, simulations of a two-dimensional cross-section of a underground four-core cable were analyzed. However, in a FEMS two dimensional simulation, the surface model is replicated along the normal's direction for a certain distance. In other words, the cable 2D cross-section is assumed to be similar all over its length. This approximation can be considered reliable for thermal aging simulations in section 4.1 since the phase conductors temperature is uniform throughout the length of the cable.

However, given that a WT is a local phenomenon, this approximation may not be as reliable as the thermal ageing case. So, to verify this proximity, 3D FEM simulations of WT faults were made and compared with the results from section 4.2.

5.1 3D FEM Model Definition

The 3D model used for these simulations was developed based on the two-dimension model presented in chapter 3. This development is divided into some steps, which will be approached individually.

5.1.1 Cable Extrusion

The first step consists in the extrusion of figure 3.1 cross-section for 20 mm. The result of this extrusion is an undamaged power cable where one of the ends is inserted in the plane $z = 0\,\text{mm}$ and the other in $z = 20\,\text{mm}$, which is presented in figure 5.1.

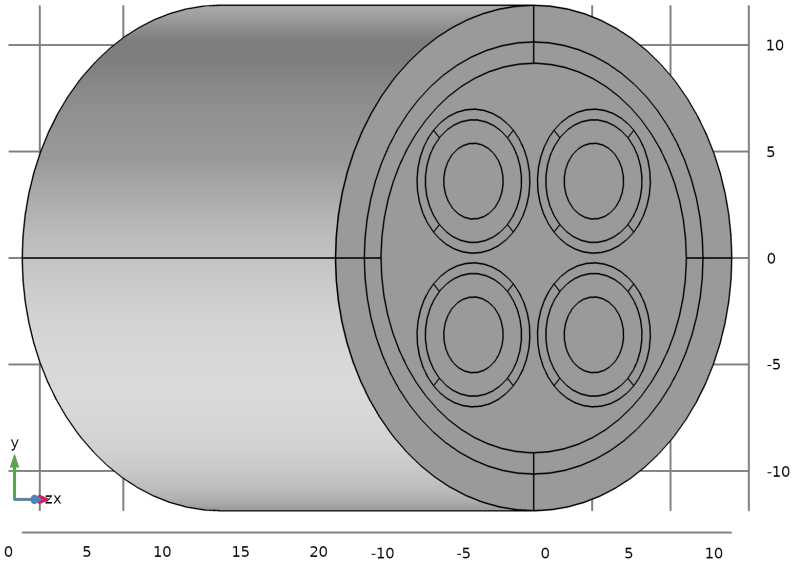

Figure 5.1: 3D model after cross-section extrusion

5.1.2 *Water Tree* Addition

After the global model of the power cable was defined, the WT was introduced. For this, a new sketch plane was created, and in it, it was drawn a semi-ellipse, as it is represented in figure 5.2.

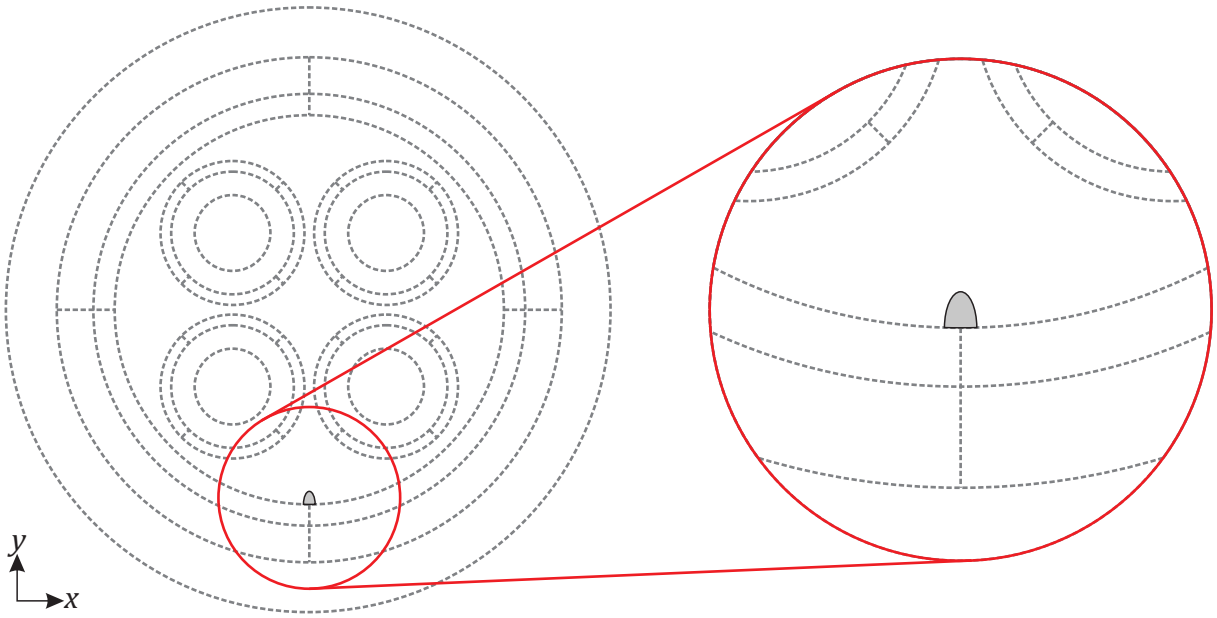

Figure 5.2: *Water tree* sketch definition

To note that, in figure 5.2, the dotted lines are not present in the WT sketch, they are just auxiliary to show the relative position of the WT in the cable. Another aspect to have in mind is the fact that the WT location in this sketch will be changed to simulate different damaged zones.

The next step in the addition of the WT was the extrusion of its sketch. This extrusion has a length of h along Z and was made in a way that it would be placed in the middle of cable length. This way, the sketch's plane would be placed in $z = 10 - h/2$ and extruded to the $z = 10 + h/2$ plane, as figure 5.3 schematic shows.

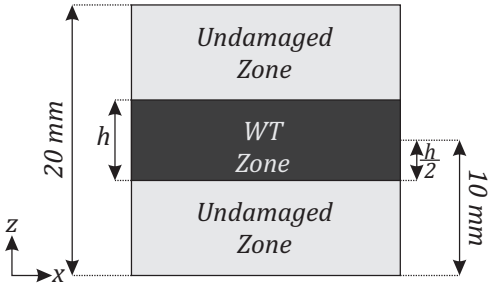

Figure 5.3: 3D Model Scheme

In figure 5.4 there's a screenshot of the FEMS cable's geometry after the addition of the WT, whose domain is highlighted in blue. Also, some of the geometry's parts were hidden, so it could be possible to

visualize the WT.

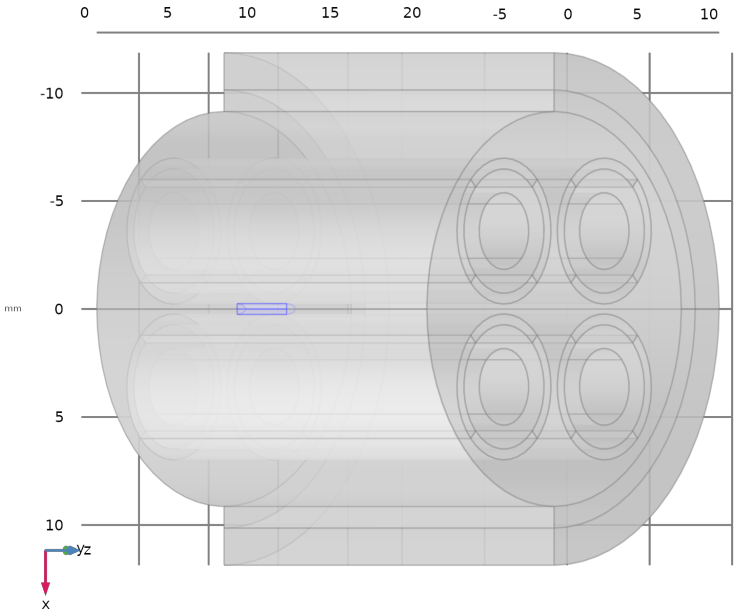

Figure 5.4: 3D model after *water tree* addition

5.1.3 Materials and Imposed Conditions

Once the model's geometry was finished, materials with specific characteristics were assigned to each domain developed. This assignment was identical to the one used in the 2D model, which is summarized in figure 3.1 and table 3.1. For the WT's domain, it was assigned XLPE and its relative electric permittivity was changed to 3.0 or 3.7 accordingly to section 2.3.2.B, and depending on simulation.

The imposed conditions were the definition of the ground and the electric potential forced in each of the phase conductors and the neutral conductor.

The ground was assigned to the outer surface of the air element, as represented in figure 5.5, where this condition is highlighted in dark blue and the air domain in light blue. To note, that the air domain is defined as an infinite element, which means that the FEMS will assume that the ground surface will be much further from the cable than figure 5.5 suggests.

For the imposition of the electric potentials, first, it was necessary to identify the conductors, which was done similarly to the 2D model, and it is presented also in figure 5.5. Having that, a pure sinusoidal three-phase balanced system was applied to the conductors as expressed in (5.1). It should also be noted that although these impositions were applied to the whole domain of the conductors, the probes used to acquire the sheats' voltages were defined in the conductors' surfaces where $z = 20\,\text{mm}$.

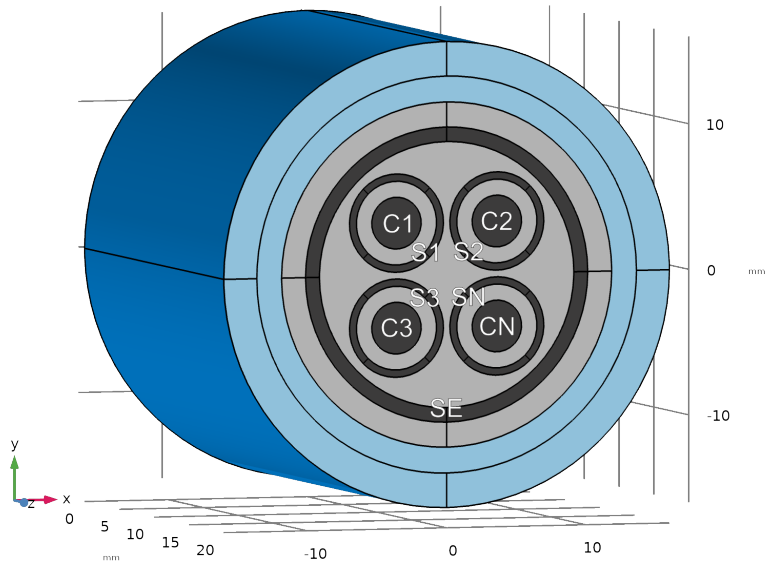

Figure 5.5: 3D model imposed conditions

$$\begin{cases} V_{C_1} = 230\sqrt{2}\cos\left(2\pi 50t\right) \\ V_{C_2} = 230\sqrt{2}\cos\left(2\pi 50t + \frac{2\pi}{3}\right) \\ V_{C_3} = 230\sqrt{2}\cos\left(2\pi 50t - \frac{2\pi}{3}\right) \\ V_{C_N} = 0 \end{cases} \quad [\text{V}] \tag{5.1}$$

5.2 Reference Simulation

Having the model defined, a simulation of an undamaged cable with no WT, (h=0 mm), was made to get reference results that will be compared with the following simulations' results. These reference parameters are presented in table 5.1.

In figure 5.6 there is also a graph depicting the norm of the electric field in a power cable cross-section located at the middle of the cable, this is, the plane with the equation $z = 10\,\text{mm}$. This plane is coincident with the centre of the WTs in the simulations where they exist, so, it's possible to visualize the differences in the behaviour of the electric field when a WT is present.

Table 5.1: 3D FEM Model reference results

$\boldsymbol{\alpha}[^\circ]$	$\boldsymbol{\beta}[^\circ]$	$\boldsymbol{a}$[V]	$\boldsymbol{b}$[V]	$\boldsymbol{x_0}$[V]	$\boldsymbol{y_0}$[V]	$\boldsymbol{\theta}[^\circ]$
43.19	55.61	281.68	257.56	-0.62	-0.38	-59.28

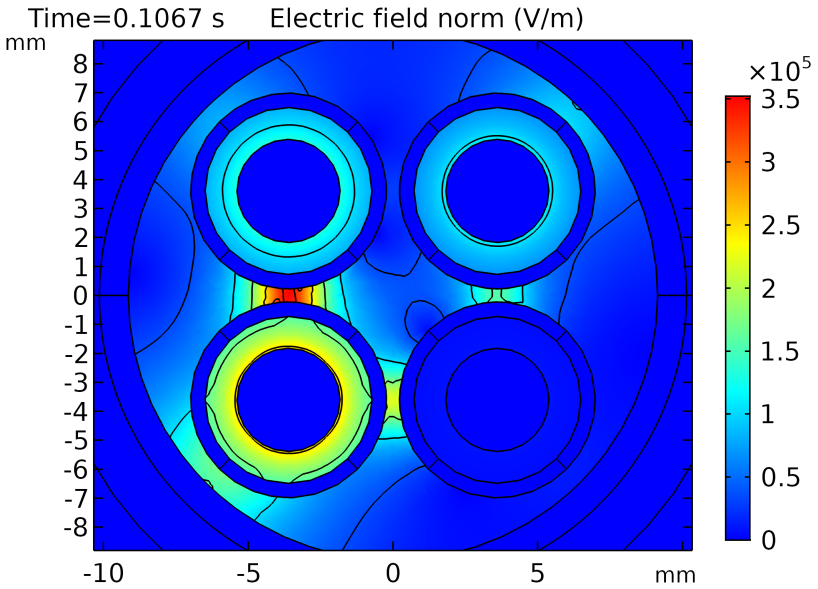

Figure 5.6: Electric field norm in a cable cross-section in the reference simulation

5.3 *Water Trees* Simulation

To check the proximity between the 2D and the 3D model results, the WT location study, presented in section 4.2, was replicated for the new model. For this, it was assumed a WT Zone thickness of h=3 mm, as represented in figure 5.7, then, simulations have been run for the same WT locations and the electric permittivities ($\epsilon_{WT} = 3.0$ and $\epsilon_{WT} = 3.7$).

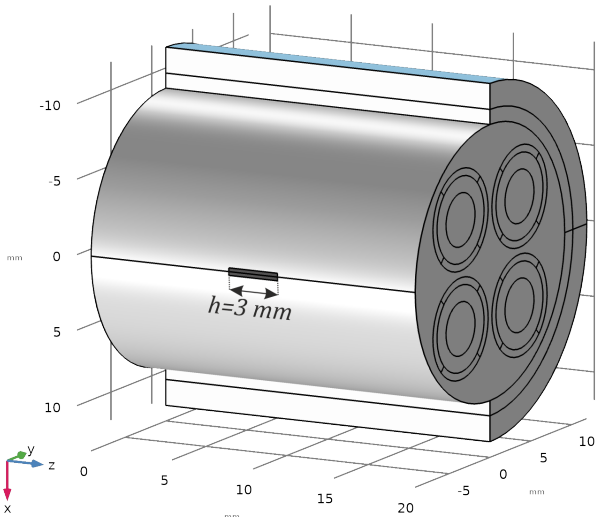

Figure 5.7: *Water Tree* length representation in 3D model

To get a physical representation of what's happening in the presence of a WT, the figures 5.8 and 5.9

shows the electric field norm in the power cable cross-section at $z = 10\,\text{mm}$ when the imposed voltage in conductor 3 is at it's maximum, for the cases where the WT is located at $-90°$ and $-135°$, respectively.

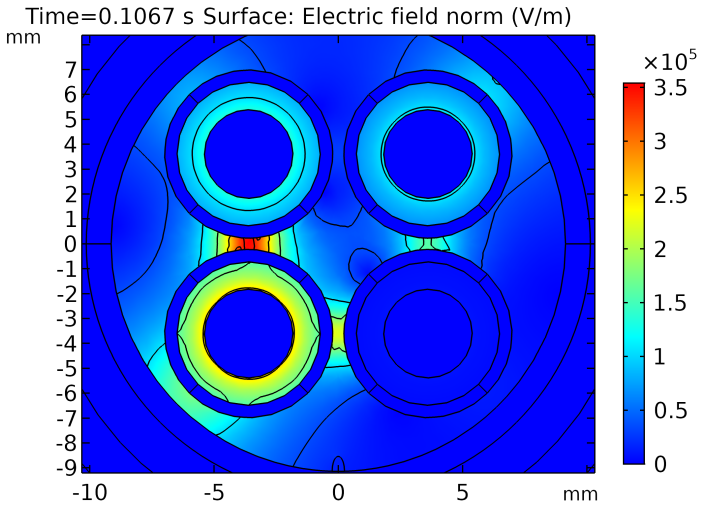

Figure 5.8: Electric field norm at $z = 10\,\text{mm}$ for a *water tree* located at $-90°$

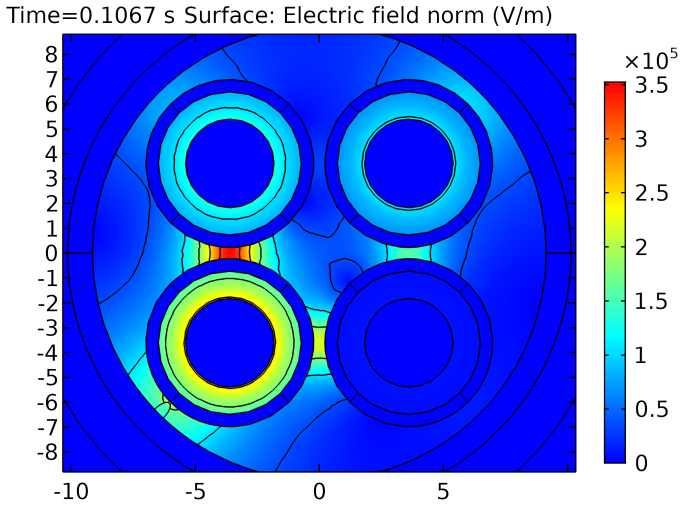

Figure 5.9: Electric field norm at $z = 10\,\text{mm}$ for a *water tree* located at $-135°$

Figures 5.8 and 5.9 are both from the worst-case simulation, this is, the case where the WT has an average relative electric permittivity of 3.7. By inspecting and compare them with the figure 5.6, it does not seem to have a difference between the WT located at $-90°$ and the reference case. However, when the WT is at $-135°$, an electric field line appears in the tip of the WT, representing a divergence in the electric field that may influence the potential in the phase 3 sheath's potential.

The results are summarized in tables 5.2 and 5.3. Using the same methodology, results were compared with the reference result in table 5.1, which allowed to develop tables 5.4 and 5.5 and figure 5.10

that shows the deviation based on the WT location.

Comparing the figures 4.4 and 5.10 results, it is notable that the behaviour of the lines are very different, suggesting that the results from the 2D model are not reliable. However, when looking at the values range, the values from the 3D model results are much lower. This means that the oscillations, in this case, maybe be caused by calculation errors instead of the WT. That is, the divergence in the lines behaviours can be provoked instead by the fact that the WT's size is too small to be detected in the 3D model and only oscillations due to calculation errors are visible.

Table 5.2: 3D Model *Water Tree* results for a relative electric permittivity of 3.0

$\boldsymbol{Location}[^\circ]$	$\boldsymbol{\alpha}[^\circ]$	$\boldsymbol{\beta}[^\circ]$	$\boldsymbol{a}$[V]	$\boldsymbol{b}$[V]	$\boldsymbol{x_0}$[V]	$\boldsymbol{y_0}$[V]	$\boldsymbol{\theta}[^\circ]$
-90	43.18	55.6	281.73	257.49	0.05	-0.06	-58.88
-112.5	43.19	55.6	281.64	257.53	-0.06	-0.22	-58.93
-135	43.19	55.61	281.74	257.56	-0.11	-0.06	-58.84
-157.5	43.19	55.6	281.65	257.52	-0.38	-0.15	-58.94
-180	43.18	55.59	281.66	257.64	0.11	-0.6	-58.36
-202.5	43.18	55.59	281.67	257.44	-0.27	-0.27	-58.9
-225	43.18	55.59	281.66	257.53	-0.39	0.06	-58.94
-247.5	43.19	55.6	281.59	257.64	-0.28	0.27	-58.92
-270	43.19	55.6	281.65	257.52	0.12	-0.09	-58.96

Table 5.3: 3D Model *Water Tree* results for a relative electric permittivity of 3.7

$\boldsymbol{Location}[^\circ]$	$\boldsymbol{\alpha}[^\circ]$	$\boldsymbol{\beta}[^\circ]$	$\boldsymbol{a}$[V]	$\boldsymbol{b}$[V]	$\boldsymbol{x_0}$[V]	$\boldsymbol{y_0}$[V]	$\boldsymbol{\theta}[^\circ]$
-90	43.18	55.6	281.71	257.55	0.14	-0.02	-58.74
-112.5	43.19	55.61	281.69	257.55	-0.56	-0.17	-59.29
-135	43.19	55.61	281.72	257.54	-0.15	0.29	-59.03
-157.5	43.18	55.59	281.64	257.56	-0.01	-0.11	-58.94
-180	43.18	55.6	281.49	257.51	0.04	0.12	-59.16
-202.5	43.19	55.61	281.77	257.48	-0.22	-0.15	-59.18
-225	43.19	55.59	281.74	257.61	-0.21	0.21	-59.09
-247.5	43.18	55.59	281.62	257.68	0.16	-0.13	-58.61
-270	43.19	55.61	281.67	257.58	0.05	0.07	-59.11

Table 5.4: 3D Model parameter deviation for a relative electric permittivity of 3.0

$\boldsymbol{Location}[^\circ]$	$\boldsymbol{\alpha}[\%]$	$\boldsymbol{\beta}[\%]$	$\boldsymbol{a}[\%]$	$\boldsymbol{b}[\%]$	$\boldsymbol{x_0}[\%]$	$\boldsymbol{y_0}[\%]$	$\boldsymbol{\theta}[\%]$
-90	-0.02	-0.03	0.02	-0.03	-108.75	-84.9	-0.68
-112.5	-0.01	-0.02	-0.02	-0.01	-90.43	-40.08	-0.6
-135	0	-0.01	0.02	0	-81.88	-84.92	-0.75
-157.5	-0.01	-0.02	-0.01	-0.02	-39.21	-59.24	-0.59
-180	-0.03	-0.04	-0.01	0.03	-117.48	60.5	-1.55
-202.5	-0.02	-0.03	-0.01	-0.05	-56.71	-29.2	-0.64
-225	-0.03	-0.04	-0.01	-0.01	-37.36	-114.92	-0.59
-247.5	-0.01	-0.01	-0.03	0.03	-55.04	-171.19	-0.62
-270	-0.01	-0.02	-0.01	-0.01	-119.73	-76.9	-0.54

Table 5.5: 3D Model parameter deviation for a relative electric permittivity of 3.7

$\boldsymbol{Location}[°]$	$\boldsymbol{\alpha}[\%]$	$\boldsymbol{\beta}[\%]$	$\boldsymbol{a}[\%]$	$\boldsymbol{b}[\%]$	$\boldsymbol{x_0}[\%]$	$\boldsymbol{y_0}[\%]$	$\boldsymbol{\theta}[\%]$
-90	-0.02	-0.03	0.02	-0.03	-108.75	-84.9	-0.68
-112.5	-0.01	-0.02	-0.02	-0.01	-90.43	-40.08	-0.6
-135	0	-0.01	0.02	0	-81.88	-84.92	-0.75
-157.5	-0.01	-0.02	-0.01	-0.02	-39.21	-59.24	-0.59
-180	-0.03	-0.04	-0.01	0.03	-117.48	60.5	-1.55
-202.5	-0.02	-0.03	-0.01	-0.05	-56.71	-29.2	-0.64
-225	-0.03	-0.04	-0.01	-0.01	-37.36	-114.92	-0.59
-247.5	-0.01	-0.01	-0.03	0.03	-55.04	-171.19	-0.62
-270	-0.01	-0.02	-0.01	-0.01	-119.73	-76.9	-0.54

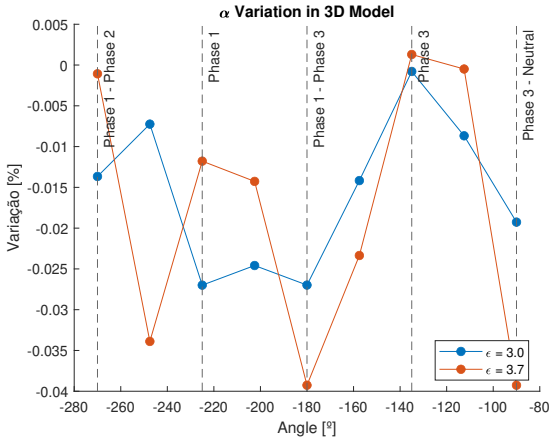

(a) Evolution of α

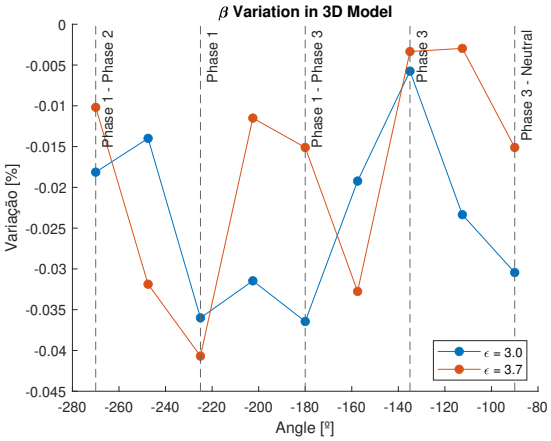

(b) Evolution of β

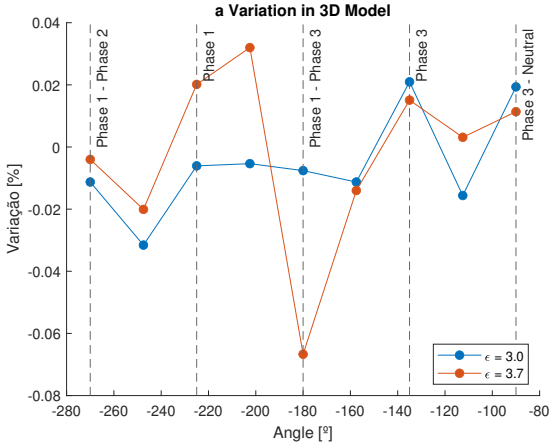

(c) Evolution of a

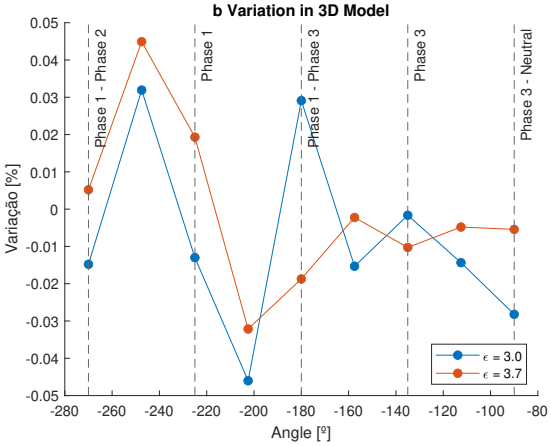

(d) Evolution of b

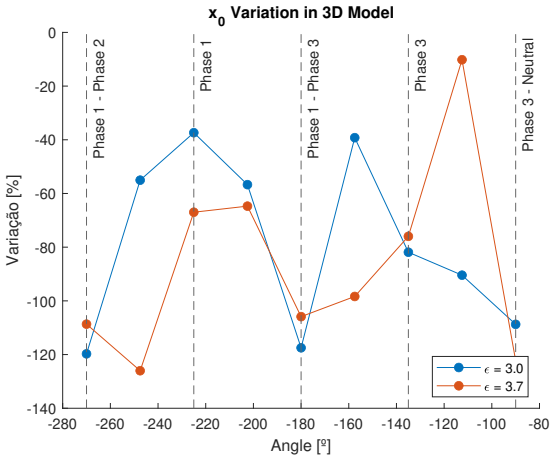

(e) Evolution of x_0

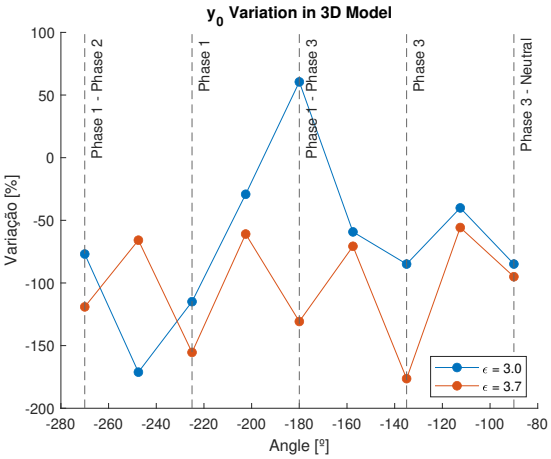

(f) Evolution of y_0

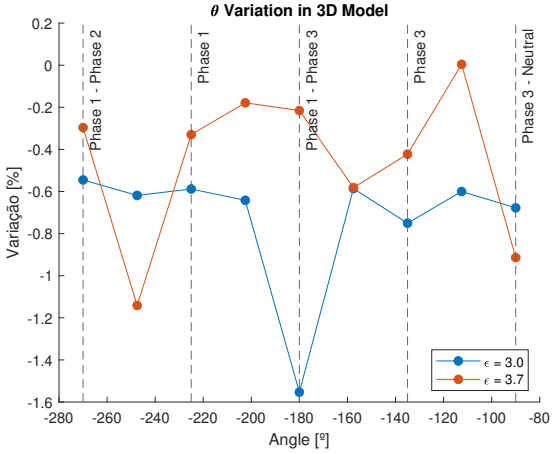

(g) Evolution of θ

Figure 5.10: Ellipse parameters evolution with *water tree* location in 3D model

5.4 *Water Tree* Size Simulation

To study the influence of the WT's size, various simulations where only the WT's dimension was changed were made. When it comes to the WT's location, initially it was chosen the region nearest to phase 3 conductor, since it's the region where a WT is more easily detected. However, two more zones were tested: the region between Phase 3 and Neutral, at $-90°$, and the region between Phase 3 and Phase 1, at $-180°$. For all the cases, the relative electric permittivity assigned to the WT's domain was 3.7.

Considering the WT's representation in this model is a prism, as shown in figure 5.11, it's volume can be changed through the base area or prism's height. So, to study also which prism's characteristics have more influence in the results, simulations have been run with the following sizes.

1. $V = 0.7\,\text{mm}^3$ ($A = 0.23\,\text{mm}^2$, $h = 3\,\text{mm}$) - Default;
2. $V = 2.1\,\text{mm}^3$ ($A = 0.69\,\text{mm}^2$, $h = 3\,\text{mm}$);
3. $V = 2.1\,\text{mm}^3$ ($A = 0.23\,\text{mm}^2$, $h = 9\,\text{mm}$);
4. $V = 4.1\,\text{mm}^3$ ($A = 0.69\,\text{mm}^2$, $h = 6\,\text{mm}$);
5. $V = 11.6\,\text{mm}^3$ ($A = 1.28\,\text{mm}^2$, $h = 9\,\text{mm}$);

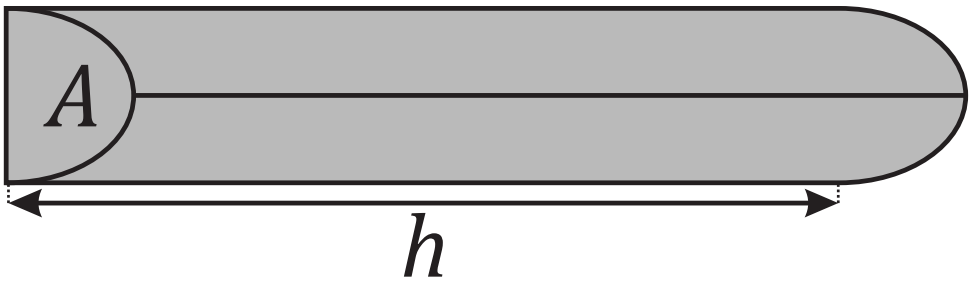

Figure 5.11: *Water tree* 3D representation

The base areas and the heights of the WTs' models used in the next simulations are scaled in two proportions, allowing to better visualize the difference between the various sizes: one for the base areas in figures 5.12 and other for the height in figure 5.13.

Figure 5.12: Base sizes for WT's size simulation

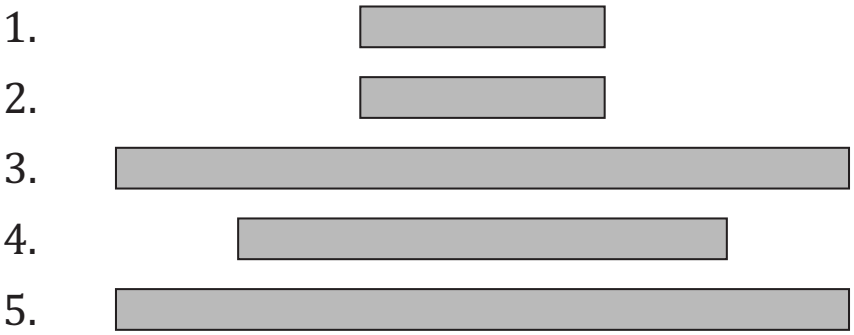

Figure 5.13: Models' height for WT's size simulation

5.4.1 Close to Phase Conductor 3 ($-135°$)

In this case, the WT is inserted in the nearest region to conductor 3, which is at $-135°$. To better visualize the concerned location, in figure 5.14, there is a representation of part of the model, where the WT, with the size of the case 1, is highlighted in red.

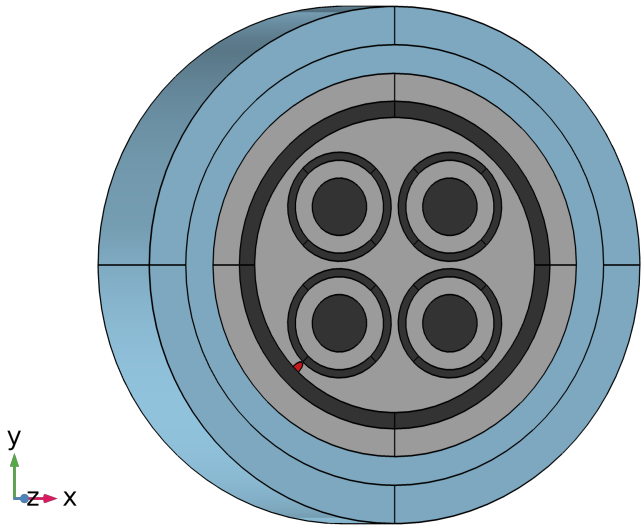

Figure 5.14: Part of the model for the WT's size simulation at $-135°$

The results from these simulations are revealed in table 5.6 in absolute values and in table 5.7 in the percentage of deviation from the reference simulations values presented in table 5.1. Also, in figure 5.15 is a bar graph where it's possible to visualize the difference between simulation results. In this figure, each colour represents one of the five cases, and each bar represents one parameter, allowing to have a better perspective on how the parameters change with the WT's size and which parameters are more affected. Since there are different ranges of variation, the seven parameters were distributed into three sub-graphs, to maintain visible the differences in the parameters with lower variations.

Table 5.6: Absolute results from close to phase conductor 3 *water tree* size study

#	V[mm^3]	A[mm^2]	h[mm]	α[°]	β[°]	a[V]	b[V]	x_0[V]	y_0[V]	θ[°]
1	0.7	0.23	3	43.19	55.61	281.72	257.54	−0.15	0.29	−59.03
2	2.1	0.69	3	43.19	55.62	281.78	257.68	−0.1	−0.14	−58.77
3	2.1	0.23	9	43.19	55.62	281.73	257.79	0	−0.01	−58.68
4	4.1	0.69	6	43.19	55.63	281.79	257.99	0	−0.06	−58.39
5	11.6	1.28	9	43.2	55.66	281.91	258.71	0	−0.01	−57.72

Table 5.7: Relative results from close to phase conductor 3 *water tree* size study

#	V[mm^3]	A[mm^2]	h[mm]	α[%]	β[%]	a[%]	b[%]	x_0[%]	y_0[%]	θ[%]
1	0.7	0.23	3	0	0	0.02	−0.01	−75.96	−176.37	−0.42
2	2.1	0.69	3	0	0.01	0.04	0.05	−83.38	−61.67	−0.87
3	2.1	0.23	9	0	0.02	0.02	0.09	−100.26	−98.42	−1.01
4	4.1	0.69	6	0	0.03	0.04	0.17	−100.8	−84.38	−1.51
5	11.6	1.28	9	0.01	0.08	0.08	0.45	−100.42	−96.58	−2.63

From these results, it's notable that the higher the WT's volume is, the higher will be the parameters variation. Also, by comparing cases 2 and 3, it's possible to conclude that a WT height (h) increase has more influence when compared to an equal increment in the base area.

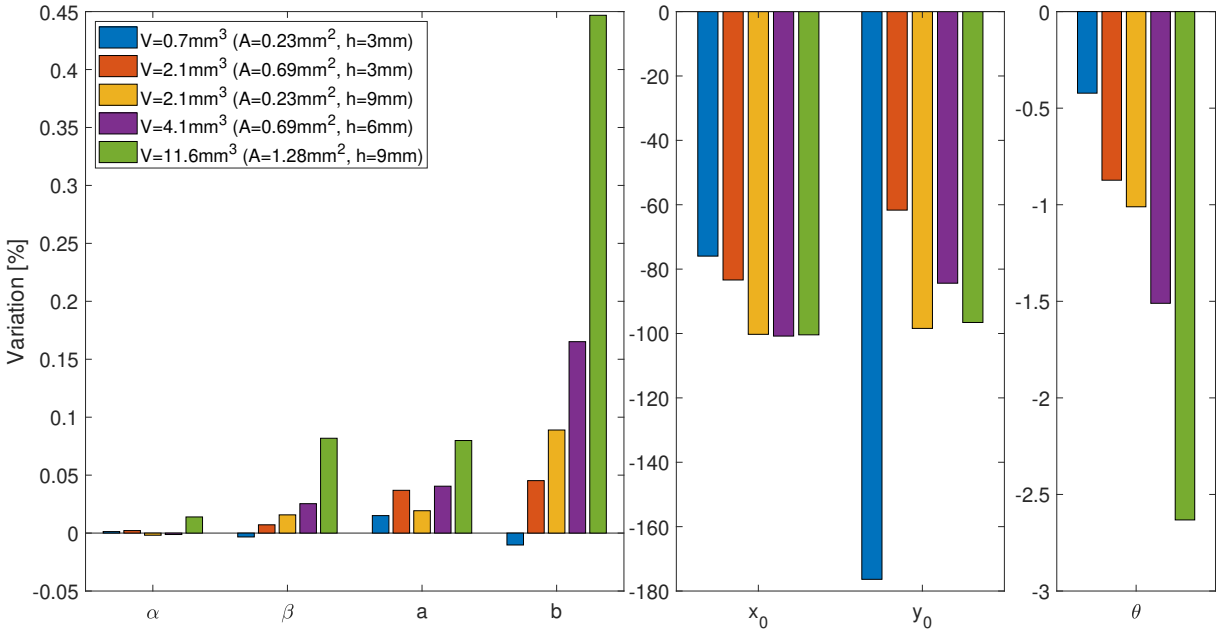

Figure 5.15: Close to phase conductor 3 *water tree* size study results' bar graph

Finally, but not less important, is the fact that the trend of the various parameters' deviation with the WT size matches the results from the two-dimensional model, presented in section 4.2. The parameters that have a higher deviation in these results are the same that have more reliable peaks in figure 4.4 at $-135°$ location, meaning that the results from section 4.2 are trustworthy. So, the disagreement between the results from 2D and 3D models is due to the WT's size used in the second case being too small to be

detected. This aspect gets a particular impact on the 3D model because the WT only affects a fraction of the power cable length. For example, the case where the WT has a height of $h = 3\,\text{mm}$ corresponds only to a portion of $15\,\%$ of the power cable length ($20\,\text{mm}$). When in the 2D model, the FEMS assumed the WT was all over the cable length.

5.4.2 Between Phase Conductor 3 and Neutral ($-90°$)

For this case, the WT is equidistant to conductor 3 and neutral, at $-90°$. Similar to the previous case, a schematic where the WT is highlighted is present in figure 5.16.

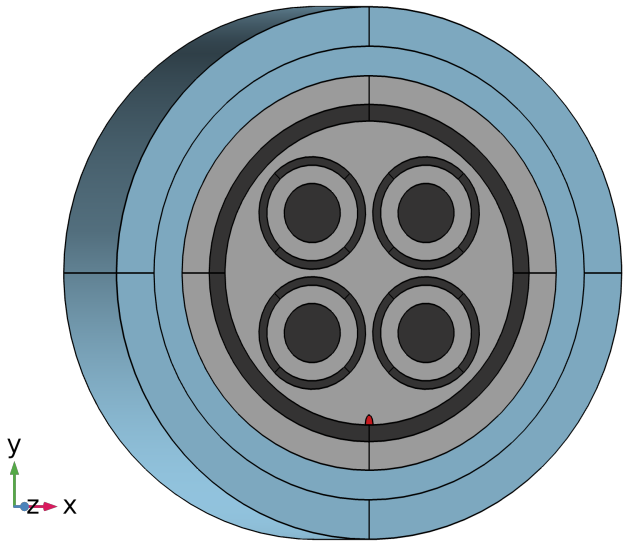

Figure 5.16: Part of the model for the WT's size simulation at $-90°$

The results from the simulations made with a WT located at $-90°$ are expressed in tables 5.8 and 5.9 and figure 5.17. By inspecting figure 5.17, it's visible that the amplitudes of deviations are much lower for this case. Also, there's not an apparent trend of evolution with the WT's volume increase, indicating the impossibility to detect a damaged region in this zone, like the 2D model simulations.

Table 5.8: Absolute results from *water tree* size study located between phase 3 and neutral

#	$\boldsymbol{V}$[mm^3]	$\boldsymbol{A}$[mm^2]	$\boldsymbol{h}$[mm]	$\boldsymbol{\alpha}$[°]	$\boldsymbol{\beta}$[°]	$\boldsymbol{a}$[V]	$\boldsymbol{b}$[V]	$\boldsymbol{x_0}$[V]	$\boldsymbol{y_0}$[V]	$\boldsymbol{\theta}$[°]
1	0.7	0.23	3	43.18	55.6	281.71	257.55	0.14	−0.02	−58.74
2	2.1	0.69	3	43.18	55.61	281.6	257.53	−0.17	−0.23	−58.94
3	2.1	0.23	9	43.18	55.62	281.67	257.43	−0.65	−0.5	−58.91
4	4.1	0.69	6	43.18	55.59	281.76	257.51	0.22	−0.36	−58.6
5	11.6	1.28	9	43.18	55.59	281.74	257.44	0.28	−0.7	−58.33

Table 5.9: Relative results from *water tree* size study located between phase 3 and neutral

#	V[mm^3]	A[mm^2]	h[mm]	α[%]	β[%]	a[%]	b[%]	x_0[%]	y_0[%]	θ[%]
1	0.7	0.23	3	−0.04	−0.02	0.01	−0.01	−122.28	−95.02	−0.91
2	2.1	0.69	3	−0.02	−0.01	−0.03	−0.01	−73.36	−39.37	−0.58
3	2.1	0.23	9	−0.02	0.01	0	−0.05	4.75	33.79	−0.63
4	4.1	0.69	6	−0.03	−0.04	0.03	−0.02	−136.04	−3.38	−1.16
5	11.6	1.28	9	−0.03	−0.04	0.02	−0.05	−144.46	86.78	−1.61

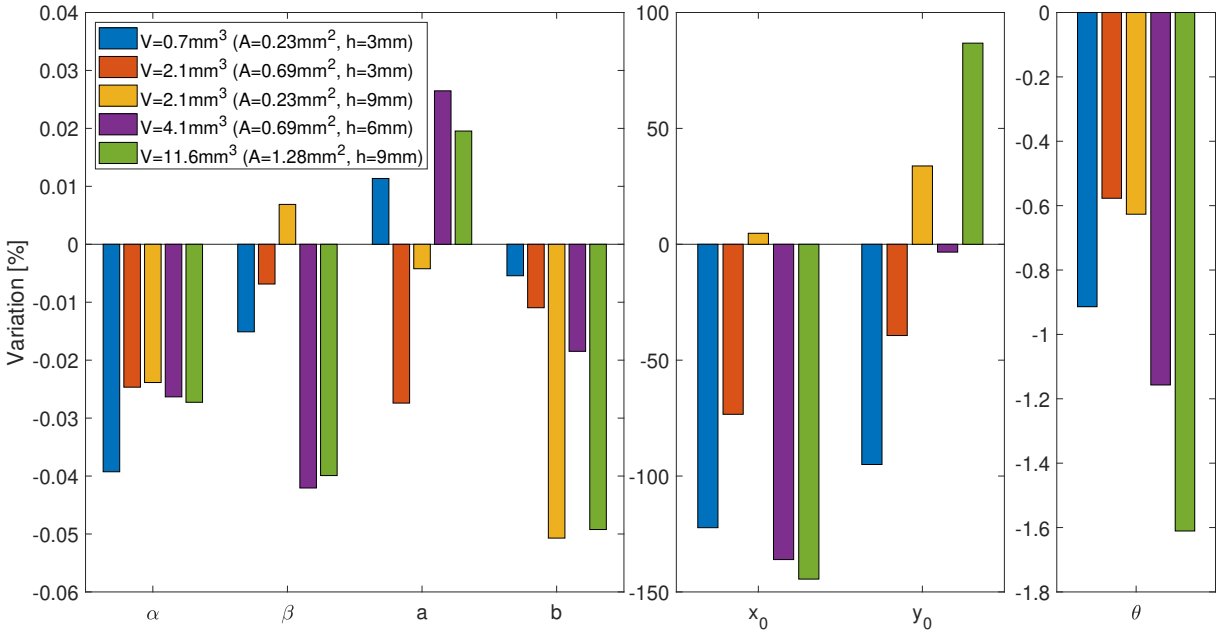

Figure 5.17: Results' bar graph for *water tree* size study located between phase 3 and neutral conductor

5.4.3 Between Phase Conductor 3 and Phase Conductor 1 ($-180°$)

For the case where the WT is located at $-180°$, with the scheme presented in figure 5.18, the simulation's results are in tables 5.10 and 5.11, in absolute and relative values, respectively. These results are also presented in the figure 5.19 bar graph.

Like the previous case, there's no apparent trend for any parameter with the increase of the WT. Also, the range of these values is similar between these two cases. This range is so small that approximation errors start to be dominant, creating a dubious zone of results where no conclusions can be made, just like the WT simulations in the 2D model at this location, in section 4.2.

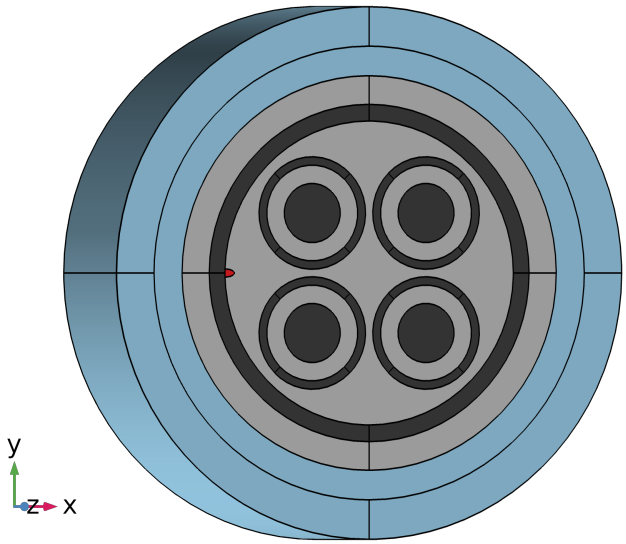

Figure 5.18: Part of the model for the WT's size simulation at $-180°$

Table 5.10: Absolute results from *water tree* size study located between phase 3 and phase 1

#	V[mm^3]	A[mm^2]	h[mm]	α[°]	β[°]	a[V]	b[V]	x_0[V]	y_0[V]	θ[°]
1	0.7	0.23	3	43.18	55.6	281.49	257.51	0.04	0.12	−59.16
2	2.1	0.69	3	43.18	55.59	281.67	257.43	0.05	−0.27	−59.14
3	2.1	0.23	9	43.18	55.6	281.67	257.5	−0.17	−0.3	−58.51
4	4.1	0.69	6	43.18	55.6	281.65	257.49	−0.23	−0.64	−58.52
5	11.6	1.28	9	43.19	55.61	281.74	257.47	0.05	−0.43	−58.95

Table 5.11: Relative results from *water tree* size study located between phase 3 and phase 1

#	V[mm^3]	A[mm^2]	h[mm]	α[%]	β[%]	a[%]	b[%]	x_0[%]	y_0[%]	θ[%]
1	0.7	0.23	3	−0.04	−0.02	−0.07	−0.02	−105.88	−130.75	−0.22
2	2.1	0.69	3	−0.02	−0.03	0	−0.05	−107.53	−27.21	−0.23
3	2.1	0.23	9	−0.04	−0.02	0	−0.03	−72.12	−18.97	−1.3
4	4.1	0.69	6	−0.04	−0.02	−0.01	−0.03	−63.47	70.14	−1.29
5	11.6	1.28	9	0	−0.01	0.02	−0.04	−108.41	13.37	−0.57

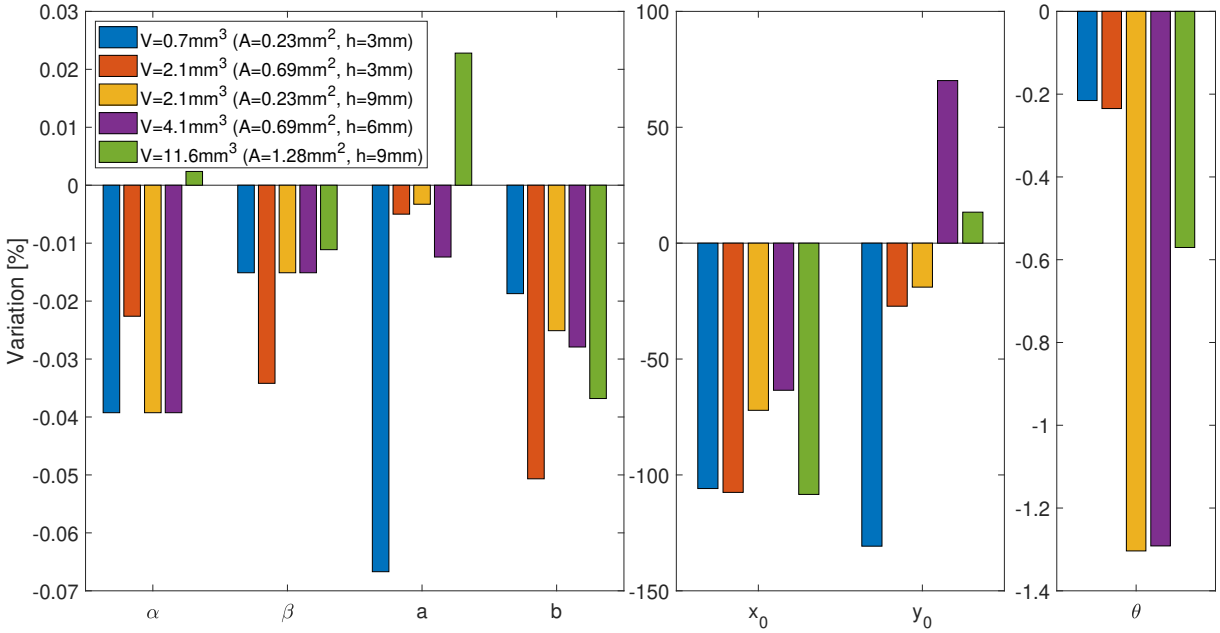

Figure 5.19: Results' bar graph for *water tree* size study located between phase 3 and phase 1

5.5 Water Tree Growth Direction

The last two sets of simulations, in section 5.4.2 and 5.4.3, are simulations where the WT's position belong to the critical group III. As defined in section 4.2, the locations from critical group III are the farthest from the conductors and have the particularity of having two conductors at the same distance.

Having in mind that the WT's grows in the direction of the electric field [12], since the electric field points in the direction of the conductor, as fig. 5.20 shows, the WT's in these locations will evolve towards one of the conductors. So, new simulations where the growth direction of this WT was changed, were developed.

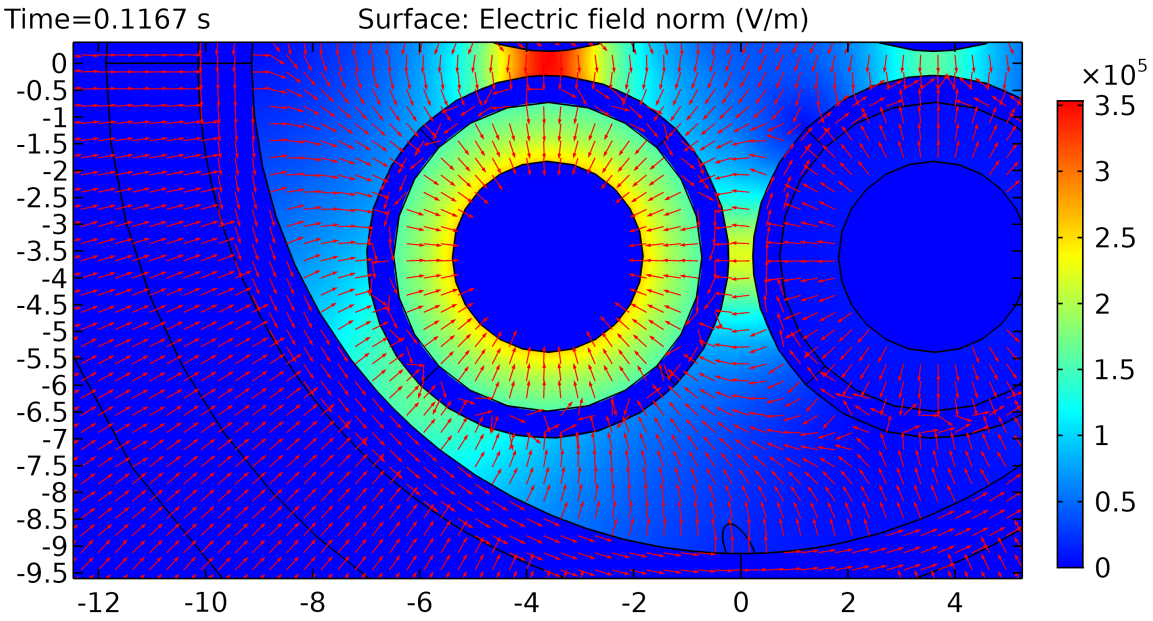

Figure 5.20: Electric field direction

Assuming γ as the angle between the direction of propagation of the water tree and the radial line which intersects the WT's root as shown in figure 5.21 scheme, γ was set to an amplitude of $30°$ and to point in the direction of phase 3 conductors.

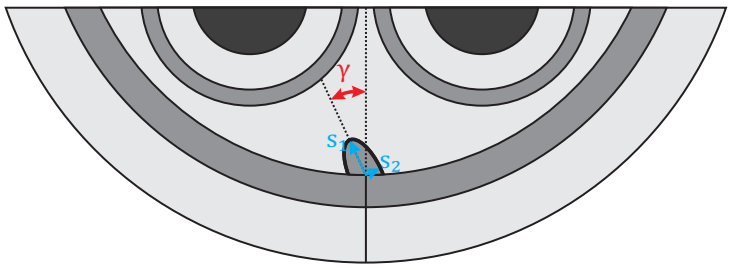

Figure 5.21: Water tree growth direction scheme

Then, simulations were made for the locations of $-90°$ and $-180°$ with the same WT representation but with different sizes. In this case, to verify also the possibility of these WTs become detectable as they get closer to phase conductors, the WTs' dimensions in these simulations were the following:

1. $S_1 = 0.6\,\text{mm}$; $S_2 = 0.25\,\text{mm}$; $h = 3\,\text{mm}$;
2. $S_1 = 1.2\,\text{mm}$; $S_2 = 0.50\,\text{mm}$; $h = 6\,\text{mm}$;
3. $S_1 = 2.4\,\text{mm}$; $S_2 = 0.50\,\text{mm}$; $h = 6\,\text{mm}$;
4. $S_1 = 2.4\,\text{mm}$; $S_2 = 0.50\,\text{mm}$; $h = 9\,\text{mm}$;
5. $S_1 = 3.2\,\text{mm}$; $S_2 = 0.50\,\text{mm}$; $h = 9\,\text{mm}$;

5.5.1 Between Phase Conductor 3 and Neutral ($-90°$)

In this case, the WT's root is in the halfway zone from phase 3 and neutral conductors, at $-90°$ location. Like the previous cases, the results of this study are presented in absolute, in table 5.12, and relative values, in table 5.13. Also, there's a bar graph, in figure 5.22, where it is possible to visualize the divergences between the seven parameters of the five simulations.

Table 5.12: Absolute results from water tree growth study locate between phase 3 and neutral

#	s_1[mm]	s_2[mm]	h[mm]	α[°]	β[°]	a[V]	b[V]	x_0[V]	y_0[V]	θ[°]
1	0.6	0.25	3	43.18	55.6	281.77	257.46	0.3	−0.44	−58.42
2	1.2	0.5	6	43.18	55.6	281.73	257.42	0.03	−0.25	−58.85
3	2.4	0.5	6	43.19	55.6	281.66	257.65	0.03	−0.18	−59.04
4	2.4	0.5	9	43.19	55.61	281.77	257.49	−0.04	−0.22	−59.06
5	3.2	0.5	9	43.19	55.61	281.7	257.66	−0.02	−0.02	−58.88

Table 5.13: Relative results from water tree growth study locate between phase 3 and neutral

#	s_1[mm]	s_2[mm]	h[mm]	α[%]	β[%]	a[%]	b[%]	x_0[%]	y_0[%]	θ[%]
1	0.6	0.25	3	−0.04	−0.03	0.03	−0.04	−148.85	17.8	−1.46
2	1.2	0.5	6	−0.04	−0.02	0.02	−0.06	−104.5	−33.09	−0.74
3	2.4	0.5	6	0	−0.02	−0.01	0.03	−104.12	−52.85	−0.42
4	2.4	0.5	9	0	−0.01	0.03	−0.03	−93.02	−40.13	−0.37
5	3.2	0.5	9	0	0	0.01	0.04	−96.54	−95.53	−0.68

After inspecting the output results, the variation ranges are pretty small, like all the simulations of WTs located at this place. Also, there's no visible trend which may indicate a relation between the output variables and the WT's dimension, meaning that these WTs are not detectable.

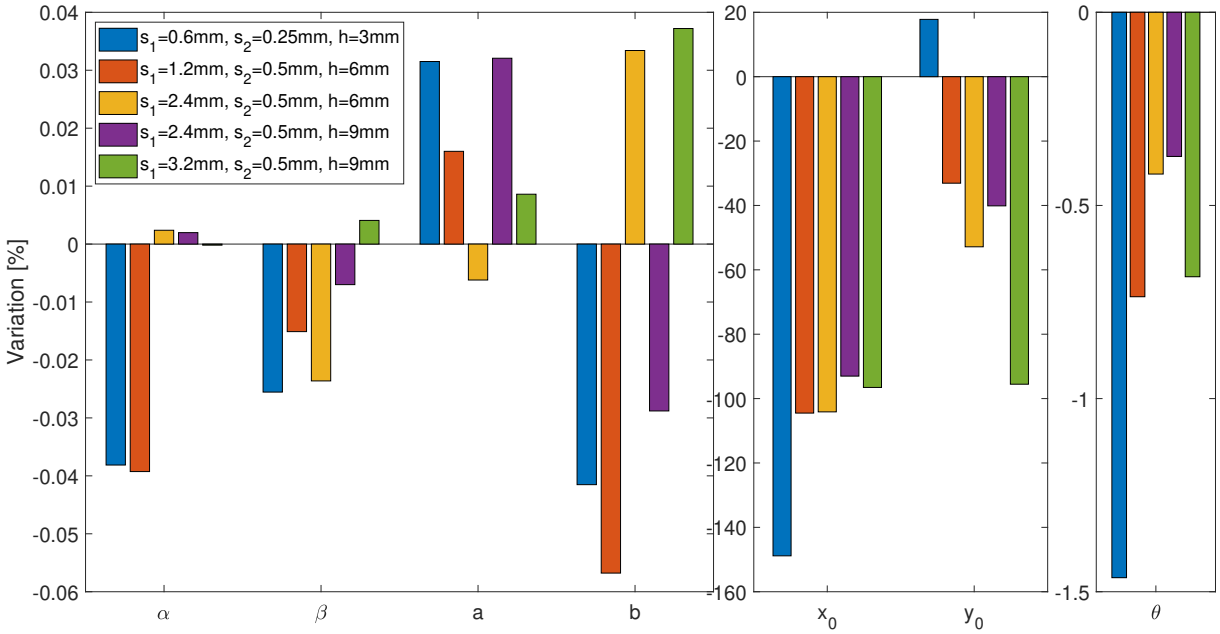

Figure 5.22: Rotated water tree at $-90°$ bar graph results

5.5.2 Between Phase Conductor 3 and Phase Conductor 1 ($-180°$)

When the WT's root between phase 1 and phase 3 conductors, at $-180°$, and the WT grows in the direction of phase 3 conductors, the output results are the ones presented in table 5.14 and 5.15, in absolute and relative values, respectively. The relative results are also presented in fig. 5.23 bar graph.

Table 5.14: Absolute results from water tree growth study locate between phase 1 and phase 3

#	s_1[mm]	s_2[mm]	h[mm]	α[°]	β[°]	a[V]	b[V]	x_0[V]	y_0[V]	θ[°]
1	0.6	0.25	3	43.18	55.6	281.46	257.58	-0.22	-0.3	-59.05
2	1.2	0.5	6	43.18	55.6	281.66	257.5	0	0	-58.93
3	2.4	0.5	6	43.19	55.61	281.74	257.51	0.04	0.09	-59.11
4	2.4	0.5	9	43.19	55.61	281.7	257.6	-0.05	-0.09	-58.85
5	3.2	0.5	9	43.19	55.61	281.72	257.66	-0.02	0.02	-58.87

Table 5.15: Relative results from water tree growth study locate between phase 1 and phase 3

#	s_1[mm]	s_2[mm]	h[mm]	α[%]	β[%]	a[%]	b[%]	x_0[%]	y_0[%]	θ[%]
1	0.6	0.25	3	-0.04	-0.02	-0.08	0.01	-64.69	-19.25	-0.39
2	1.2	0.5	6	-0.02	-0.02	-0.01	-0.02	-100.34	-98.81	-0.6
3	2.4	0.5	6	0	0	0.02	-0.02	-105.64	-124.9	-0.3
4	2.4	0.5	9	-0.01	0	0.01	0.01	-91.53	-74.97	-0.73
5	3.2	0.5	9	0	0	0.01	0.04	-96.54	-104.98	-0.69

The panorama of these results is similar to the previous case. There is no apparent trend of the parameter's evolution when the WT grows in the conductor direction, and the range of values obtained is very low. Once again, the conclusion is that it is not possible to detect WTs at these locations, as it

was suggested in the simulations from section 5.3 and 5.4 and also in chapter 4.

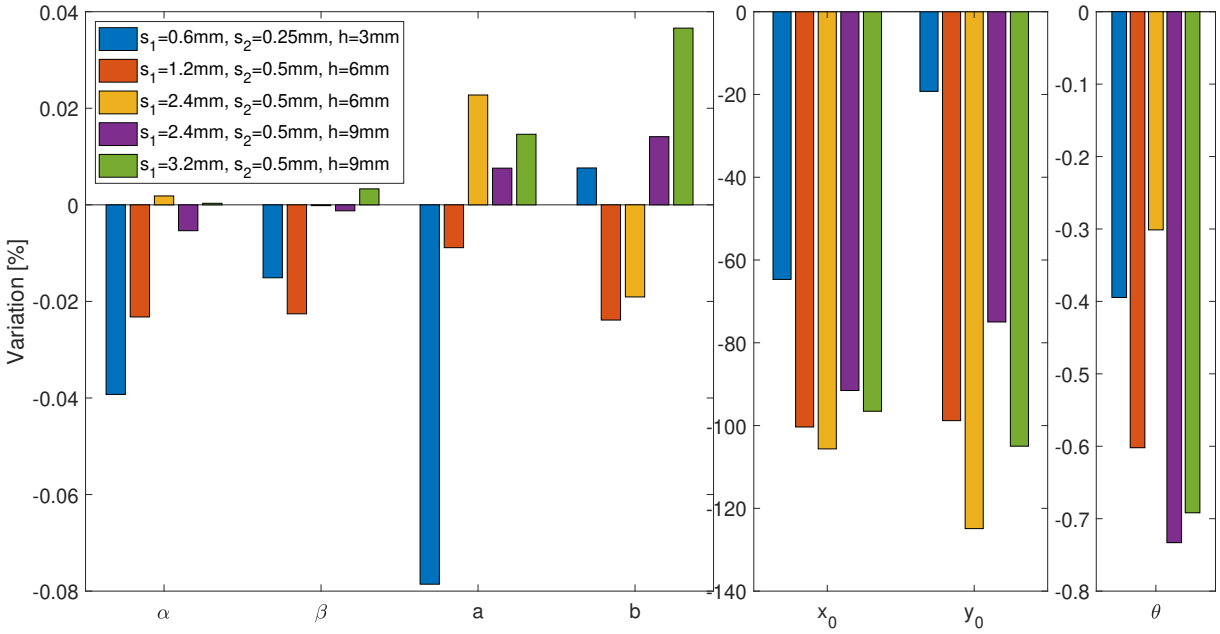

Figure 5.23: Rotated water tree at $-180°$ bar graph results

6

Analysis of the Results

Contents

In chapters 4 and 5, simulations of power cables in pre-determined conditions were made to check how some variables would change. Based on this, this chapter will do the reverse process, estimate the power cable's condition through the analysis of those variables changes. This process will be summarized in a flowchart that will be decomposed in various steps.

6.1 Thermal Ageing vs *Water Trees*

Since the simulations made can be divided into two groups of deterioration as thermal ageing and/or *water trees* occurrence, the first step will be to establish a methodology that allows distinguishing these two groups, and can be summarized into the flowchart from figure 6.1.

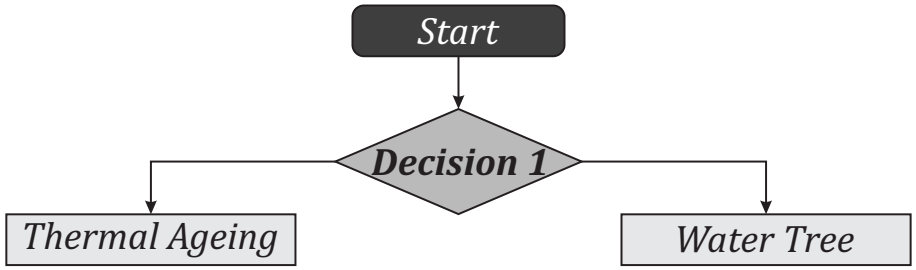

Figure 6.1: Flowchart - Selecting deterioration type

From sections 4.1 and 4.2, it was verified that the parameters more trustworthy were a and b, considering the higher deviation and the less noise in the WT simulations case. For these parameters, it was noted that for thermal ageing both a and b change in the same direction, while for the WT case, only one of these parameters changes. It was also detected that the variation of these parameters is more intense for the thermal ageing than for the WT simulations. So, the conditions from *Decision 1* block from figure 6.1 can be summarized as in table 6.1.

Table 6.1: Conditions to filter the deterioration type

Thermal Aging	**Water Tree**	
$\lvert\Delta a\rvert > 1\%$	$\Delta a > 0.1\%$	$\lvert\Delta a\rvert < 0.1\%$
$\lvert\Delta b\rvert > 1\%$	$\lvert\Delta b\rvert < 0.1\%$	$\Delta b > 0.1\%$
$\Delta a \times \Delta b > 0$	-	-

6.2 Thermal Ageing

In section 4.1, it was mentioned that the parameters variation for those simulations could also be provoked by a temperature change. So, it is necessary to estimate the real cause of this type of parameters

variation.

In case there's an increase of α, a, b and θ and a decrease of β, there's no doubt that it reflects a temperature rise. However, the opposite case, where α, a, b and θ decrease and β increase, can indicate a temperature drop or thermal ageing. Having in mind that ageing is an irreversible process and a change in temperature not, this means that although these parameters may oscillate between a range of values due to temperature changes, this range may change due to ageing, meaning that parameters will reach new values. So, a simple methodology could be recording parameters values over time. This way, when these parameters' values reached unprecedented levels, this would indicate ageing of the cable. This process is summarized in figure 6.2 flowchart, where the conditions for *Decision 2* block are expressed in table 6.2.

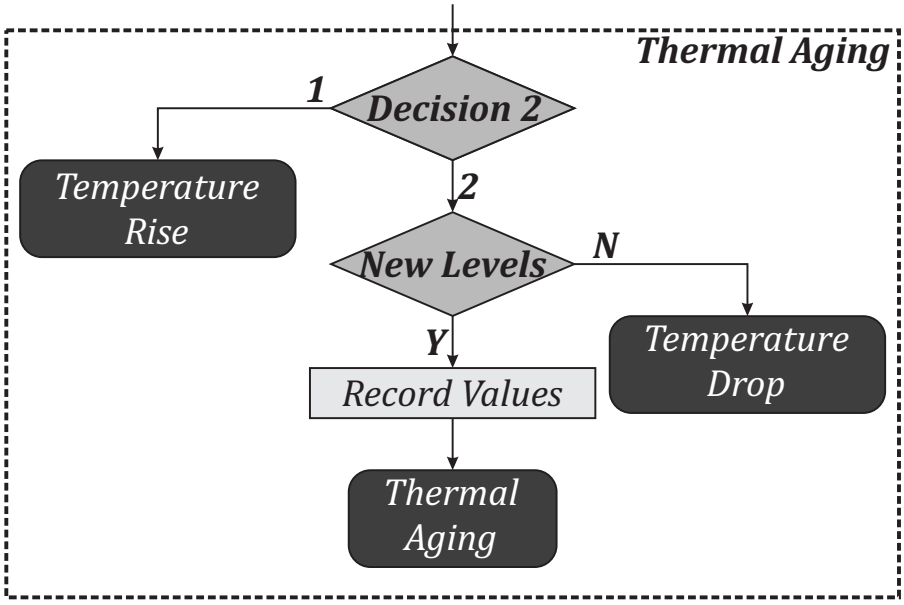

Figure 6.2: Thermal aging block flowchart

Table 6.2: *Decision 2* block conditions

Output 1	Output 2
$\Delta\alpha > 0$	$\Delta\alpha < 0$
$\Delta\beta < 0$	$\Delta\beta > 0$
$\Delta a > 0$	$\Delta a < 0$
$\Delta b > 0$	$\Delta b < 0$
$\Delta\theta > 0$	$\Delta\theta < 0$

6.3 *Water Tree*

After detecting the existence of a WT, it can be possible to estimate the location of the WT in the cable, using the same data. In section 4.2, only the WTs near conductors were detected, but, they affected the results in different ways. When near from phase 1 conductors, the parameter a has increased and the y_0 declined. When near from phase 3 conductors, parameters b, α and β has increased while θ has decreased. This pattern can be used to distinguish the nearest conductor from the affected zone through a simple check, as represented in figure 6.3, where the *Decision 3* block is summarized in table 6.3.

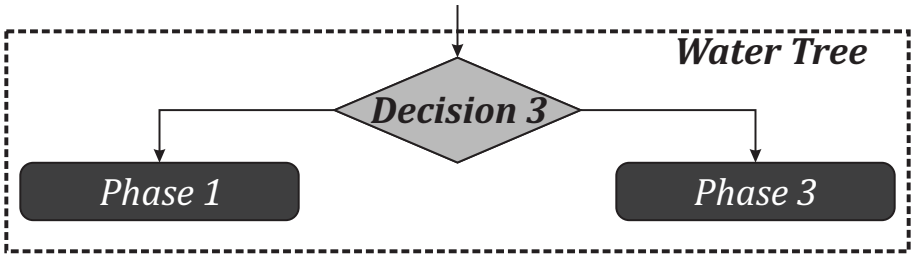

Figure 6.3: *Water tree* block flowchart

Table 6.3: *Decision 3* block conditions

Phase 1	Phase 3
$\Delta a > 0$	$\Delta b > 0$
$\Delta y_0 < 0$	$\Delta \alpha > 0$
-	$\Delta \beta > 0$
-	$\Delta \theta < 0$

These three steps, from figure 6.1 to 6.3, are merged into a single flowchart, which is located in figure 6.4, and shows in an overall view the suggested methodology to estimate the power cable's condition through the analysis of parameters' variation.

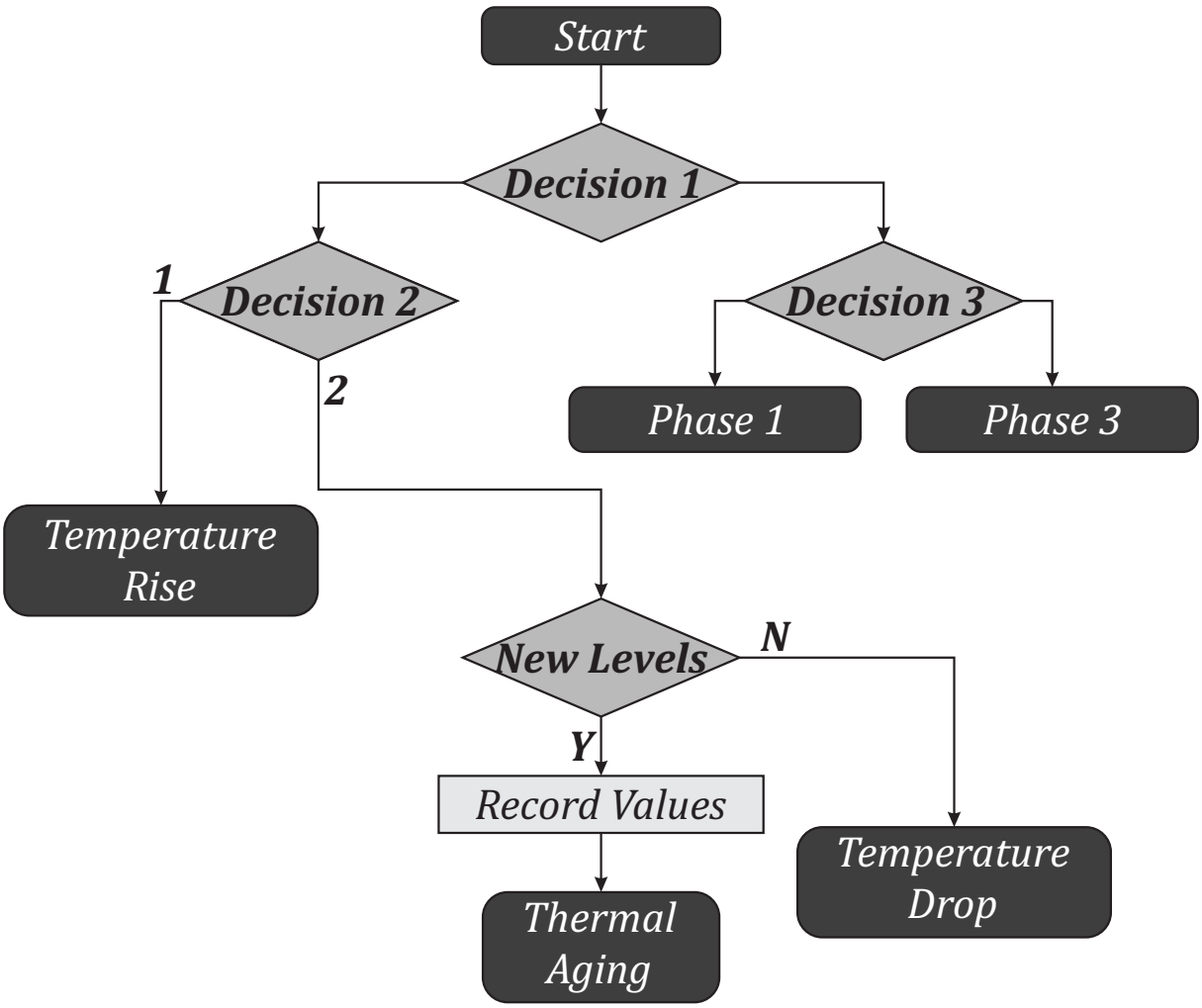

Figure 6.4: Overall flowchart

7

Conclusion

Contents

7.1 Achievements

This thesis aimed to develop an alternative methodology capable of predicting a power cable fault through a system that could be installed, without interfering, under already operating networks and based in electric variables. Some phenomenons, responsible for the degradation of this component, were studied and the simulated.

For the case of thermal ageing, the FEMS simulations allowed to detect a pattern, that could be used to identify this phenomenon based on electric variables. However, temperature variations can also cause the same pattern, so, the addition of temperature data would allow more accuracy to the proposed methodology.

This work also developed simulations for the case of the WT phenomenon, using 2D and 3D models. These simulations allowed to identify a new pattern when the WT were located in the nearest regions from phase conductors. For all the cases the variations were relatively small, but for the simulations with the smallest WTs' sizes, the output results start to be more affected by noise from the computational errors and approximations, forbidding any possible conclusion. It means that only from certain sizes the WT become detectable.

When it comes to the remaining WT's locations, additional simulations were developed to investigate a criterion that could identify them, however without success.

7.2 Future Work

Based on the exhibited work, and since it still needs developments, this section has some guidelines for future steps:

- Simulate harmonics in the applied voltages and analyze how it affects the results;
- Introduction of an acquiring system for temperature data to better distinguish the thermal ageing from the temperature variations and to have more information from operation conditions;
- Analyze how is the soil's moisture in the surrounding region of a power cable and how it can vary with weather phenomena and then highlight WTs.

To note that these guidelines are just suggestions and are targeted to the phenomenons studied in this work. Other occurrences and other purposes can be studied and would contribute to the value of the proposed.

Bibliography

[1] G. Chen and C. H. Tham, "Electrical treeing characteristics in XLPE power cable insulation in frequency range between 20 and 500 Hz," *IEEE Transactions on Dielectrics and Electrical Insulation*, vol. 16, no. 1, pp. 179–188, 2009.

[2] Q. Chen, E. Makram, and X. Xu, "A hybrid high frequency pulse and pattern recognition method for water tree detection in long distance underground cables," *IEEE Power and Energy Society General Meeting*, vol. 2015-Septe, no. January, 2015.

[3] Y. Mecheri, L. Boukezzi, A. Boubakeur, and M. Lallouani, "Dielectric and mechanical behavior of Cross-Linked Polyethylene under thermal aging," *Conference on Electrical Insulation and Dielectric Phenomena (CEIDP), Annual Report*, vol. 2, pp. 560–563, 2000.

[4] I. Radu, M. Acedo, J. C. Filippini, P. Notingher, and F. Frutos, "The effect of water treeing on the electric field distribution of XLPE: Consequences for the dielectric strength," *IEEE Transactions on Dielectrics and Electrical Insulation*, vol. 7, no. 6, pp. 860–868, 2000.

[5] B. Lanz and E. Sanchez, "Is Fault Location Killing Our Cable Systems?" *Proceedings of the IEEE Power Engineering Society Transmission and Distribution Conference*, vol. 2016-July, pp. 0–4, 2016.

[6] T. S. Sidhu and Z. Xu, "Detection of incipient faults in distribution underground cables," *IEEE Transactions on Power Delivery*, vol. 25, no. 3, pp. 1363–1371, 2010.

[7] J. A. Faria, *Electromagnetic Foundations of Electrical Engineering*. Willey, 2008.

[8] N. M. and K. V., *High Voltage Engineering*. The McGraw-Hill Companies, 2009, no. 1.

[9] P. H. Moon, "The Theory of Thermal Breakdown of Solid Dielectrics," *Transactions of the American Institute of Electrical Engineers*, vol. 50, no. 3, pp. 1008–1021, 1931.

[10] N. Parkman, "Electrical breakdown by tracking," *Proceedings of the IEE - Part B: Electronic and Communication Engineering*, vol. 109, no. 22S, pp. 448–453, 1962.

[11] S. Konglysan and W. Rungseevijitprapa, “XLPE Insulated High Voltage Underground Cable Assessment of Leakage Current Studies,” *International Journal of Computing, Communication and Instrumentation Engineering*, vol. 2, no. 2, pp. 162–164, 2015.

[12] T. Boonraksa, N. Promvichai, T. Supanarapan, K. M. Minja, P. V. Chombo, and B. Marungsri, “Simulation of Electric Field Distribution in Water Treed XLPE HV Underground Cable Using COMSOL Multiphysics,” in *Proceedings of the IIAE International Conference*, 2017, pp. 267–270.

[13] R. G. Cabrera, A. G. Parada, J. A. Gordillo-Sosa, J. Q. Domínguez, and M. B. Adame, “System of Measurement and Analysis of Partial Discharges in Underground Power Cables,” *International Journal of Computer and Electrical Engineering*, vol. 7, no. 6, pp. 399–407, 2015.

[14] Y. J. Han, H. M. Lee, and Y. J. Shin, “Thermal aging estimation with load cycle and thermal transients for XLPE-insulated underground cable,” *Annual Report - Conference on Electrical Insulation and Dielectric Phenomena, CEIDP*, vol. 2017-Octob, pp. 205–208, 2018.